RESEARCH ARTICLE
doi:10.59236/geomorphica.v2i1.50

GEOMORPHICA

Physical and Mechanical Properties of a New Analog Material (MAT-V) for Geomorphic Experiments

Stéphane Dominguez [*1], **Romain Sylvain** [2], **Clément Garcia-Estève** [1], **Rodolphe Cattin** [1], **Fabien Graveleau** [2]

[1]Univ. Montpellier, CNRS, Laboratoire Géosciences Montpellier, Montpellier, France , [2]Univ. Lille, CNRS, Univ. Littoral Côte d'Opale, Laboratoire d'Océanologie et de Géosciences, Lille, France

Author contributions: *Data curation*: S. Dominguez, R. Sylvain, C. Garcia-Estève, R. Cattin. *Formal Analysis*: S. Dominguez, R. Sylvain, C. Garcia-Estève, R. Cattin, F. Graveleau. *Funding acquisition*: R. Cattin, S. Dominguez. *Resources*: S. Dominguez, R. Cattin. *Software*: R. Cattin, C. Garcia-Estève. *Visualization*: S. Dominguez, R. Sylvain, R. Cattin, C. Garcia-Estève. *Writing original draft*: S. Dominguez, R. Sylvain, R. Cattin, C. Garcia-Estève, F. Graveleau. *Writing, review and editing*: S. Dominguez, R. Sylvain, R. Cattin, C. Garcia-Estève, F. Graveleau.

Abstract The experimental study of interactions between tectonics and surface processes is an ambitious challenge, requiring the development of specific analog materials capable of jointly simulating geomorphological and crustal deformation processes. In this work, we refined the physical and mechanical properties of the MAT-IV analog material to improve morphological rendering and extend its range of application. We halved the average particle size (D_{50}) of the granular mixture and added a fifth component (pumice powder), which increased the material's erodibility and allowed the precipitation rate controlling exogenous surface processes to be reduced by a factor of three. We performed a dozen experiments to explore different compositions and determine a standard formula through morphometric analyses. The new material, MAT-V, allows for reproducing better-scaled morphologies and represents a significant upgrade over MAT-IV. Scaling analysis and morphometric measurements lead to the recommended composition: 37.5% silica microbeads (1–50 µm grain size), 37.5% silica powder (1–80 µm grain size), 15% PVC powder (5-85 µm grain size), 10% pumice powder (1–150 µm grain size), < 1% anthracite (0–200 µm grain size). Using an average cyclic rainfall rate of 5–10 mm/h, a spatial scaling of 1 cm = 100 m and 1 s = 5 years are considered relevant to model relief dynamics under temperate to sub-tropical climatic conditions. To constrain the key parameters governing model surface dynamics, we implemented a joint modeling approach combining experimental and numerical modeling. This allowed us to quantify geomorphological parameters, including the slope (n) and discharge (m) exponents, hillslope erodibility (K_{hill}), critical slope (S_c), and effective settling velocity (V_s).

† ***Non-english abstract available:*** *A French abstract is published online.*

Received:
January 06, 2025
Accepted:
October 24, 2025
Published:
March 19, 2026

Editor-in-Chief:
Alice Lefebvre
Associate Editors:
Batbaatar Jigjidsuren
Anonymous AE2
Managing Editor:
Xun Yang
Copy Editor:
Nari Miller
Production Editor:
Ayobami Abegunrin;
Vittoria Vandelli

Reviewers:
Anonymous Reviewer 1
Anonymous Reviewer 2
Anonymous Reviewer 3

1 Introduction

1.1 Scientific issue

Relief dynamics is controlled by strongly coupled interactions between lithospheric to crustal deformation mechanisms and geomorphic processes acting on large time and space scales (e.g., Burbank and Pinter, 1999; Bonnet et al., 2007; Tucker and Hancock, 2010; Scheingross et al., 2020). While tectonics and volcanism play the main role in the creation of new landforms or the rejuvenation of pre-existing ones, their actions are counterbalanced by surface processes that level the Earth's surface: erosion and sedimentation (e.g., Willett et al., 1993, 2006; Montgomery and Brandon, 2002; Bishop, 2007). By transferring large volumes of material from rising relief to adjacent basins, surface processes modify the state of stress in the shallow crust, and thus, the dynamic equilibria controlling mechanical couplings between deep tectonic processes and surface deformation. Erosion, by reducing normal stress, partly controls tectonic activity including fault kinematics and the propagation of the deformation (e.g., Beaumont et al., 1992; Willett, 1999; Malavieille, 2010; Steer et al., 2014). Sedimentation has a comparable effect, modifying the stress state of the crust by increasing the vertical load, leading to elastic flexure or isostatic readjustments (e.g., Beaumont, 1978; Watts et al., 1982; Garcia-Castellanos and Cloetingh, 2012). It also raises river base levels, reducing their incision and transport capacities and thus affecting large-scale erosion rates (e.g., Babault et al., 2005b,a). Finally, climate, in the broadest sense of the term, is a key factor to consider as it governs the intensity and cyclicity of surface geomorphological processes (e.g., Bonnet and Crave, 2003; Whipple et al., 1999; Whipple and Tucker, 1999; Whipple, 2009; East and Sankey, 2020).

1.2 Contributions and insights from analog modeling

Studying these complex couplings is therefore of major interest for understanding the morphological evo-

*Corresponding author: stephane.dominguez@umontpellier.fr

lution of natural landforms, determining the impact of tectonics and climate on relief dynamics, and assessing associated natural hazards. Given the large variety of temporal and spatial scales involved in tectonic and morphogenetic processes, experimental modeling has long been recognized as a valuable complement to field investigations. However, simulating the interactions between crustal deformation and geomorphic processes remains an ambitious challenge, implying the development of analog materials capable of jointly simulating geomorphological and geological deformation processes. For more than a decade, Graveleau and Dominguez (2008) developed a promising analog material (MAT-IV) that meets the required criteria to study Tectonic–Erosion–Sedimentation couplings in active mountain forelands (Fig. 1). This material has since been used for several PhD theses and post-doctoral studies, revealing its strengths and limitations (Graveleau, 2008; Strak, 2012; Viaplana-Muzas et al., 2015; Guerit et al., 2016; Strzerzynski et al., 2021). Recently, several international teams from Italy (Reitano et al., 2020, 2022, 2023; Conrad et al., 2023) and China (Mao et al., 2021; Yan et al., 2023) have begun using analog materials based on MAT-IV-type compositions. These works confirmed previous results and also provided new data on the properties of MAT-IV as well as new applications for the study of natural cases.

The MAT-IV composition and properties were initially designed to satisfy several physical and mechanical criteria known to drive natural relief dynamics. As stated in Graveleau et al. (2011):

- The material rheology should be dominated by the Mohr-Coulomb failure criterion to replicate the brittle deformation of the upper crust and generate associated tectonic features and processes such as faults, fractures, frictional slip, and folding.
- It should erode through diffusive and gravity-driven processes on hillslopes (sheetwash, soil creep, debris flow, landslide) and advection in valleys (vertical and lateral channel incision) to simulate the main erosion and transport processes that shape natural relief morphologies and form geomorphic features such as drainage basins, crests, hillslopes, and riverbeds.
- The grain-size distribution should be small enough and range over several orders of magnitude to ensure varying transport distances of particles and grain sorting.
- Erosion rates, which control model time scaling, should be high enough to keep the experiment duration manageable.
- Rainfall rates should be kept as low as possible to avoid excessive runoff flows on the model surface which could locally generate out-of-scale morphologies (overhanging cliffs, extensive debris flows, etc.).
- Syntectonic sedimentary deposits should be stratified to record tectonic activity and stratigraphic features such as lateral facies changes, unconformity, cut-off, and down-lap.

The original MAT-IV standard composition was made up of glass microbeads (Mb 40%), silica powder (PSi 40%), polyvinyl chloride plastic powder (PVC 20%), and some graphite (Gr 1–2%), by weight of dry material (Fig. 1). Graphite particles were added to enhance the material texture, improving the accuracy of photogrammetric DEM acquisition and model surface measurements. The MAT-IV was mixed with 20 ± 1% of water in weight to obtain a cohesive paste (saturation rate around 25%). Over the years (Fig. 1), its initial composition has evolved slightly to adapt to the different geological contexts investigated

- Graveleau et al. (2011): PSi 40%, Mb 40%, PVC 20%, Gr <1%,
- Strak et al. (2011) and Strzerzynski et al. (2021): PSi 35%, Mb 40%, PVC 23%, Gr 2%,
- Viaplana-Muzas et al. (2015, 2018) and Guerit et al. (2016): PSi 30%, Mb 46%, PVC 24%, Gr <1%.

1.3 Objectives

In recent years, we started modifying the MAT-IV analog material composition to overcome some of its identified weaknesses through improvements in its physical and mechanical properties. The present study reports on the work carried out to this end and the results obtained. Our main objectives were to increase analog material erodibility while decreasing water runoff on the model surface to:

- Densify the drainage network by enhancing channel incision and limiting mass wasting.
- Refine the fine-scale details of the modeled morphologies, including geomorphic and tectonic features (fluvial terraces, knick-points, fault scarps, etc.).
- Limit the impact of inertial forces of water flows on model morphology to avoid sapping processes.

These enhancements also intended to expand its fields of application to smaller spatial and temporal scales up to 1 cm = 100 m and 1 s = a few years, respectively.

2 Methodology

To achieve our objectives, we implemented a multidisciplinary approach to test new analog material compositions. We combined geomorphic analog modeling (Section 2.1), measurements of the physical and mechanical properties of MAT-V (Section 2.2), and joint analog/numerical modeling to constrain the material's key geomorphological parameters (Sections 2.3 and 2.4).

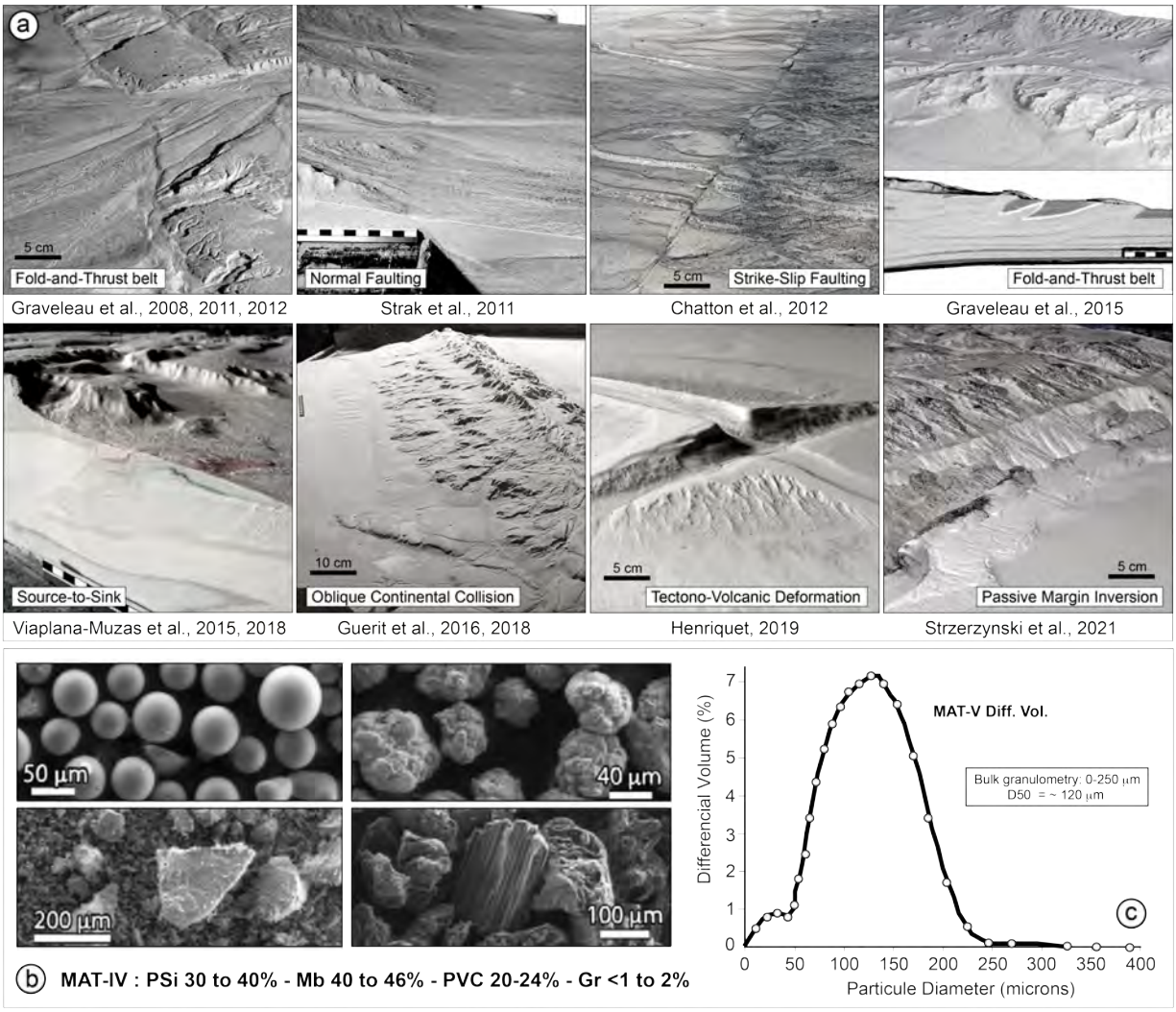

Figure 1 In the 2010s, an experimental set-up and a water-saturated analog material mixture composed of four components (MAT-IV) were developed to investigate Tectonics-Erosion-Sedimentation couplings in active mountain foreland contexts (Graveleau, 2008; Graveleau et al., 2011). Since then, MAT-IV has been used to explore many other geological settings (see Graveleau et al., 2012, 2015, for a review). **a)** References to PhD theses that used the MAT-IV analog material. **b)** Microscopic photographs of the MAT-IV components and their relative proportions in the standard composition. Psi: Silica powder, Mb: microbeads, PVC: Polyvinyl Chloride powder, Gr: Graphite powder. **c)** Typical granulometry of MAT-IV.

2.1 Analog modeling : MAT-IV to MAT-V properties evolution

2.1.1 Experimental set-up

We developed specific analog experiments to test variants of the MAT-IV formulae. The experiments were conducted at the Geosciences Analog Modeling Laboratory at the University of Montpellier (France), in the same facility where geomorphic experiments published in Graveleau (2008); Graveleau et al. (2015); Strak et al. (2011); Viaplana-Muzas et al. (2015, 2018); Guerit et al. (2016); Henriquet et al. (2019); Strzerzynski et al. (2021) were carried out. The experimental assembly is made of a reinforced aluminum frame fitted with fixed and rigid mobile plates (Figs. 2a and 2b). The model surface area measures 1.5 m x 1 m. Thrust faulting is simulated by moving the mobile plate toward the fixed ones with imposed strike and dip angles (45 ± 1°). Slip mode is controlled by a computerized mechanical device, allowing for nearly continuous micrometric to millimetric stick-slip type displacements. During the experiment, a Sony Alpha 7R2 camera (42 Mpix) captures images every 30 s to create a time-lapse movie of the experiment and to measure model surface kinematics using the sub-pixel spectral correlation method Van Puymbroeck et al. (2000). Two Panasonic Gx80 cameras, located on both sides of the model, record the morphologic evolution of the fault scarp with a 30-second time interval. To simulate climate forcing and associated erosion and sedimentation processes, four sprinklers located above the fixed plateau spray water microdroplets over the model surface. The water delivery systems have been upgraded by connecting the sprinkler's support to a motorized oscillating system to homogenize the rainfall distribution on the models.

To quantify the morphologic evolution of the experimental landscapes, stereo-photogrammetric Digital Elevation Models (DEMs) are acquired from 15 high-resolution photos (7952 x 5304 pixels, Sony Alpha 7R2 camera) covering the whole model surface (Fig. 2c) for every 5 mm of displacement along the fault plane. DEMs are processed using the MicMac software Rupnik et al. (2017) at a horizontal spatial resolution of 250 micrometers. The vertical precision depends on the local

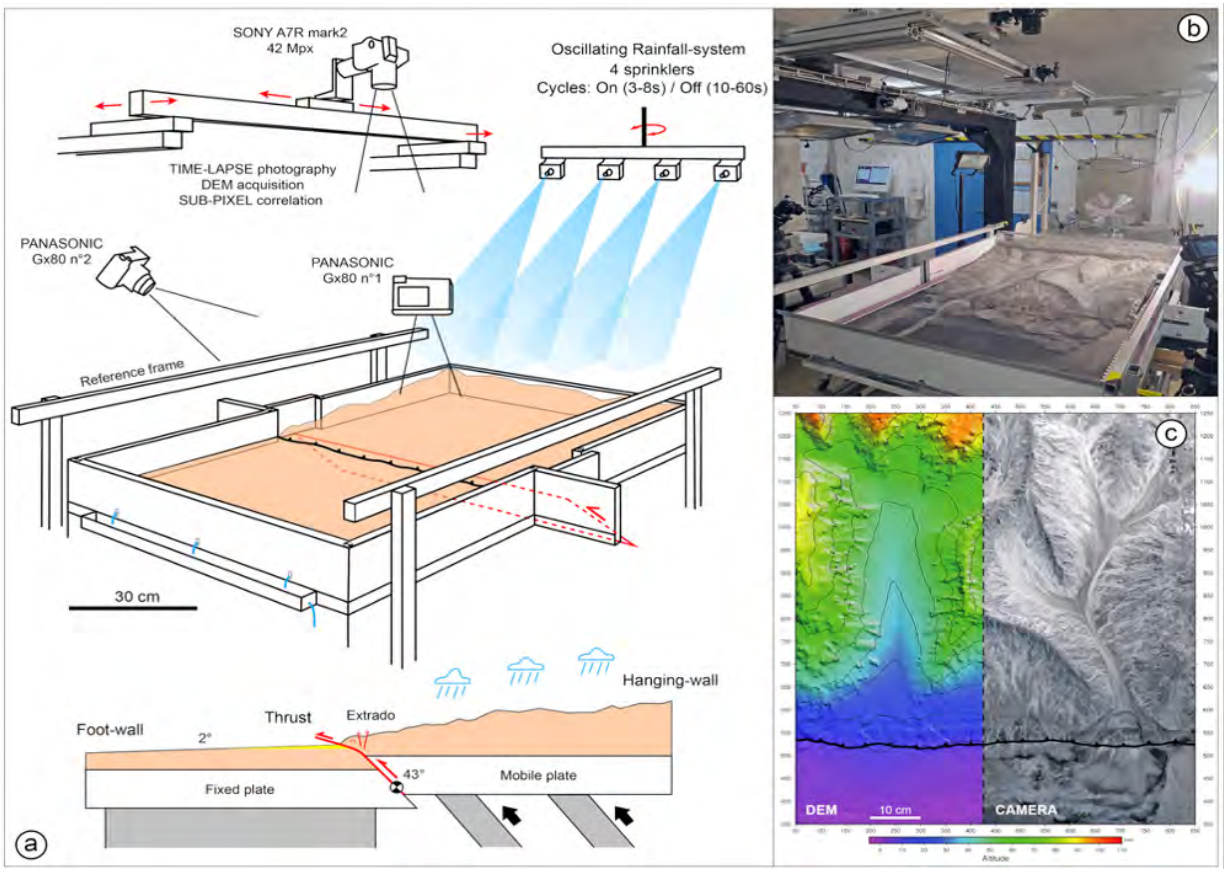

Figure 2 Experimental set-up used to test different MAT-V compositions. **a)** Schematic view of the set-up and monitoring devices. **b)** Photograph of the experimental laboratory. **c)** Examples of model morphology and the associated Digital Elevation Model (map view).

texture of the model surface, and it is estimated to be 200–300 micrometers. The experimental device is also equipped with low-angle halogen lighting and reference frames to facilitate model observation and quantitative monitoring. To enable cross-comparisons between the analog experiments, all the experiments share a similar initial topography consisting of two asymmetric watersheds extending over the whole hanging wall (mobile plateau) and a gently (2°) dipping plain extending over the footwall (fixed plateau).

2.1.2 Exploring new material compositions

We tested several combinations of material composition and climatic conditions (introducing cyclic rainfall with 4–5 s wet and 22–60 s dry periods). Based on our prior experience designing MAT-IV, we focused exclusively on ranges of analog material properties and compound proportions that yield realistic landscapes, deliberately excluding those known to produce out-of-scale morphologies (e.g., Graveleau et al., 2011; Huggett, 2016). A total of 10 successful experiments were carried out (Fig. 3). In the first experiment (EXP 1), we introduced pumice powder and reduced the grain size of the glass microbeads from 75–150 µm to 0–50 µm. Smaller microbead grain sizes make it possible to better resolve fine-scale geomorphological features, particularly the drainage network, and potentially increase transport distances. The addition of pumice powder (Pp) had a qualitative effect during the mixing of the material. Less water (-2%) was needed to reach saturation than with MAT-IV. Pp, therefore, has a water-capturing effect due to its intrinsic high porosity. This first experiment showed the influence of Pp on the material. We also replaced the graphite powder with anthracite powder (0–200 µm and D_{50} = 75 µm).

Indeed, graphite disperses freely as finer particles in contact with the water, rendering the analog material mixture darker, which locally degrades the resolution of stereophotogrammetric DEMs and sub-pixel spectral correlation. The composition of the mixture in the following experiments (EXP 2–4) remained unchanged. In these experiments, we improved the rainfall distribution over the model by making the sprinklers oscillate (Fig. 2). The dry period of the rainfall cycles was doubled for EXP 4 to lengthen the low water stage (from 30 s to 60 s). This modification was constrained by the time it takes for the last water flows to reach the fixed plateau (foreland basin). Thus, the wet period begins just as the low-water period ends. This configuration increased river incision but was not totally satisfactory since the overall erodibility of the material still appeared too low (determined qualitatively at this stage). EXP 5 is based on the same composition and climate forcings as EXP 3. We used it to assess the reproducibility of our experiments and sensitivity to slight changes in precipitation distribution. In subsequent experiments (EXP 6–9), the proportion of pumice powder was doubled (from 5% to 10%) significantly increasing the material's erodibility. Increased erosion has led to the appearance of grainy patches formed by the concentration of PVC grains, roughening the model surface. In

the EXP 7, we replaced the original PVC powder (60–250 µm, Ref: 257RF) with finer PVC (45–90 µm, Ref: 266SF). The change in PVC powder reduced the proportion of incision in favor of diffusion processes. In this experiment, the model slopes appeared smoother, and few incision markers, such as fluvial terraces, formed (Fig. 3).

After this last experiment, the main objective was to adjust the component proportions in the mixture to promote fluvial incision. Based on the behavior of MAT-IV, we knew that by decreasing the Mb/PSi mass ratio, river incision could be enhanced. In the EXP 8 experiment, we subsequently reduced the ratio of microbeads to silica powder to less than one (Mb/PSi < 1). The model exhibits steeper maximum slopes (>75°), and its overall morphology shows some similarities with bad-land-type morphologies, only observed in specific settings in nature. For the last experiment (EXP 9), we used equal proportions of Mb and Psi (Mb/PSi ratio = 1), similar to MAT-IV.

2.1.3 MAT-V best formula and key achievements

We determined that the composition giving the best results was that of experiment 9: where Mb was at 37.5%; Si, 37.5%; PVC, 14%; PP, 10%; and A, 1%). This choice was guided by the previous qualitative observations we made and first-order morphometric measurements, including topography metrics and material flow analysis. As shown in Figs. 4 and 5, erosion maps and slope distributions reflect quantitative differences in general and local model morphologies. In the first sets of models (from EXP 3 to 6), the high-frequency distribution of preserved surfaces indicated that the material erodibility was too low (Figs. 4 and 5). In these models, erosion appeared essentially dominated by channel incision, and the efficiency of diffusion processes was too limited. For EXP 7 and 8, the imbalance between incision and diffusion processes was much less pronounced, and a generalized erosion affected the whole model surface. However, these models often feature steep slopes (vertical cliffs) at the head of the catchment area and rounded crest lines, indicating that slope erosion was mainly driven by gravity instabilities. Debris flows were also often observed in this set of experiments. In EXP 9, over the whole model and along the fault zone (Figs. 4 and 5), fluvial incision was also well-expressed but less dominant. Alluvial fans appeared slightly incised, and fluvial/alluvial terraces were preserved without developing a badlands-type morphology. Remnants of the initial surfaces in EXP 9 were much less abundant than in EXP 3, 4, 5, and 6, while sharp slopes were less frequent than in EXP 7 and 8.

At this stage, we concluded that the main objectives were reached:

- The erodibility of the materials was increased while reducing the rainfall rate.
- Drainage networks appeared denser, and slope morphologies, including crest lines, were improved. The distribution of erosive processes (diffusion, incision) was well-balanced.
- Model topography appeared more detailed with finer morphologic and tectonic markers.
- No abnormal, out-of-scale morphologies caused by the inertial forces of water flows or by an overly-cohesive material were observed.

The choice of the standard composition is based on a limited set of experiments (x10) as this type of analog model is always challenging to conduct, and the model monitoring processing is time-consuming. Further experiments might have refined this standard composition by a few percent, but with limited practical significance. Indeed, natural landscapes develop on a wide range of lithologies and climatic conditions that cannot be accurately simulated using a single analog material composition. Future modelers will need to adapt the MATV composition to suit their scientific objectives and experimental setups.

2.2 Characterization of MAT-V physical and mechanical properties

The properties of the standard MAT-V composition, identified as the most suitable for investigating relief dynamics (section 2.3), were analyzed in detail. Physical (3.1) and mechanical properties (section 3.2) were determined using specific laboratory equipment and protocols, including electronic microscopy, direct shear test, micro-penetrometer, and permeameter measurements. Additionally, MAT-V morphological parameters were constrained through a combined analog and numerical modeling approach (section 3.3).

2.2.1 Physical properties

The various components of the the MAT-V, and the MAT-V mixture were imaged using an FEI Quanta 200 FEG electronic microscope at the MEA of Montpellier University (France). Results are summarized in Fig. 6a. Notably, the particles exhibit a wide range of shapes (rounded, flat, irregular), sizes, and densities. This variety promotes particle sorting within channels, resulting in variable particle transport distances, and stratified syn-kinematic deposits. We measured the Bulk MAT-V and individual components' grain size distributions at the Laboratoire d'Analyse des Sols (LAS, UNISTRA-EOS, Strasbourg, France) using a Beckman Coulter LS230 laser granulometer (Fig. 6b). The MAT-V granulometry extends from a few microns up to about 200 µm with a D_{50} close to 45–50 µm. It is more than twice as fine as MAT-IV with a D_{50} of 110–120 µm (see Fig. 1c). We calculated the MAT-V apparent density by weighing successive known volumes of material under dry, water-saturated, compacted, and uncompacted conditions (Fig. 6c, bottom left). When dry and uncompacted, the MAT-V has a low volumetric mass, close to 1 ± 0.1 g/cm^3. When compacted, dry MAT-V volumetric mass increases to 1.2 ± 0.075 g/cm^3. When mixed with approximately 21–22% water by weight, which corresponds to the stable water content where water loss occurs only by natural evaporation, its volumetric mass is 1.7 ± 0.05 g/cm^3.

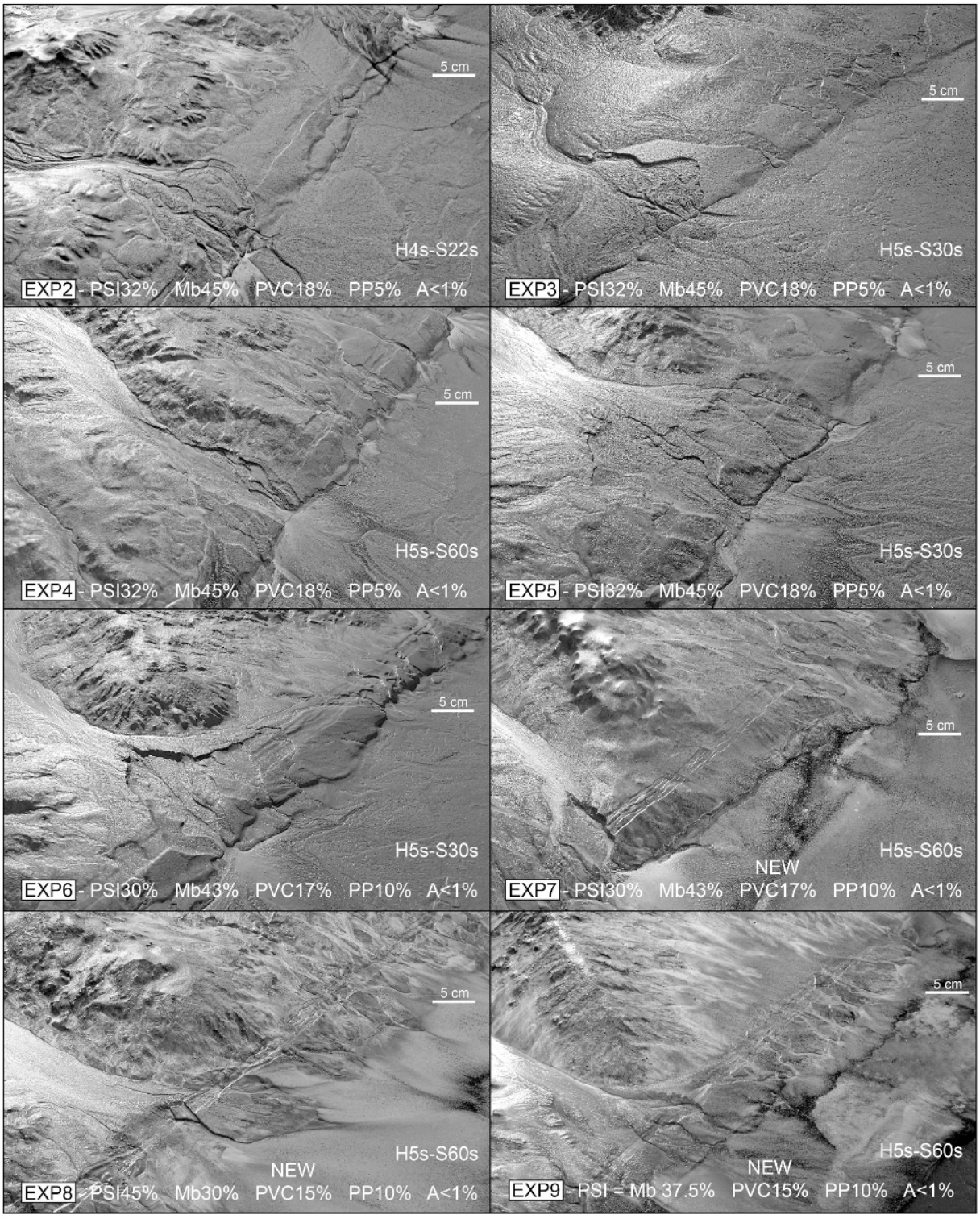

Figure 3 Selection of different final model morphologies, obtained with variable MAT-V compositions and rainfall conditions, giving relevant results. The EXP 9 model, and the associated MAT-V composition, has been considered the most similar to natural landscapes.

We quantified the MAT-V intrinsic permeability using a custom-built Darcy's pipe permeameter (Fig. 6d, bottom right). The protocol involves measuring the pressure gradient at the inlet and outlet of a cylindrical PVC cell filled with MAT-V material and subjected to increased water flow. Water is injected into the PVC cell using a precision discharge pump, crosses the material, and goes out freely at ambient pressure. Strainers, pressure equalizers, and filter paper are placed at both ends of the PVC cell to stabilize the flow line across the sample. Two pressure gauges record fluid pressure at the inlet and outlet. The observed linear relationship between discharge velocity and pressure gradient indicates that permeability follows Darcy's law. MAT-V exhibits very low permeability of ~50 mDarcy, approximately an order of magnitude lower than MAT-IV (~500 mDarcy).

2.2.2 Mechanical properties

The mechanical properties of the MAT-V are of primary importance. They not only control how it deforms un-

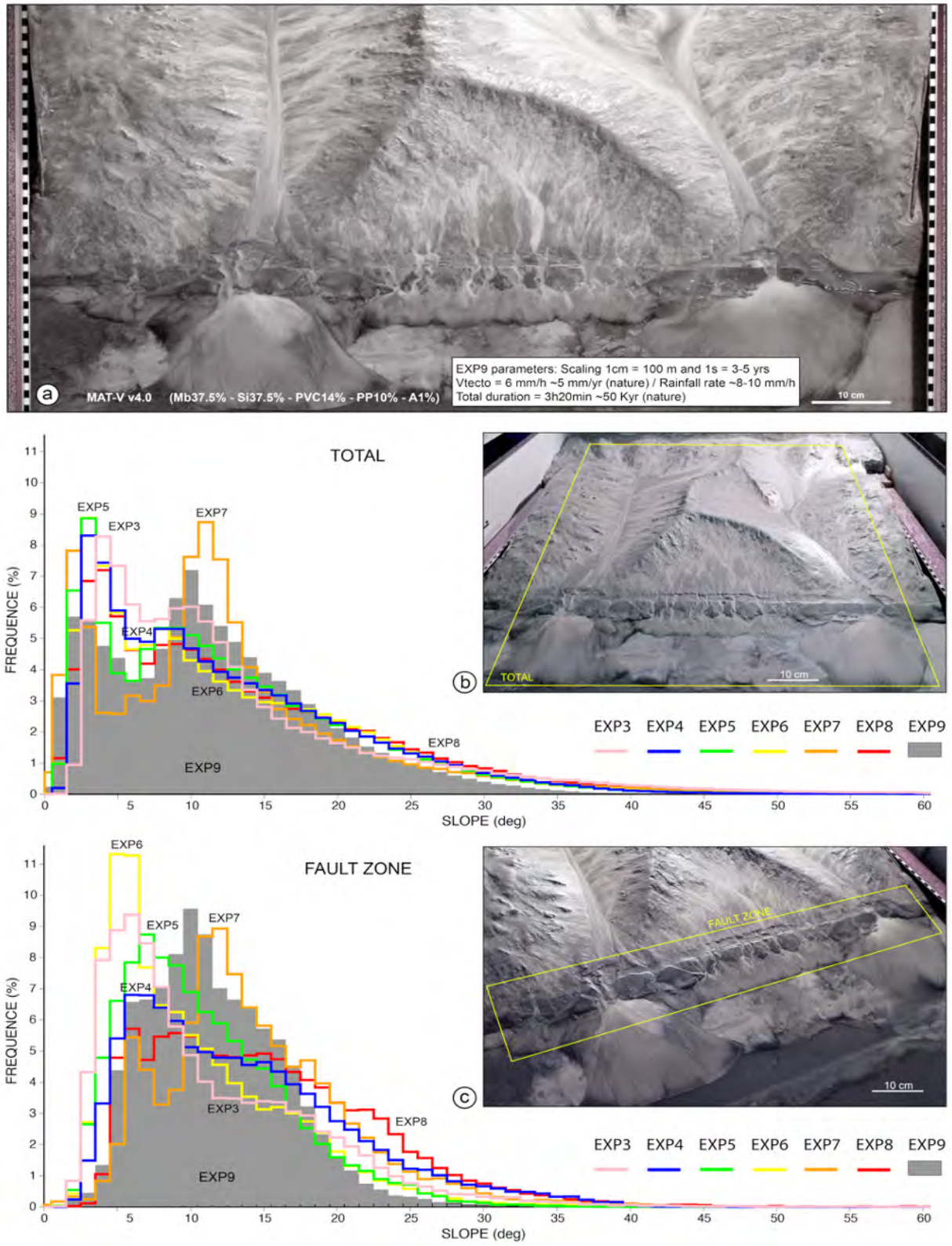

Figure 4 Example of morphometric measurements used to quantitatively determine the optimal MAT-V composition. **a)** General 2D view of the final stage of EXP 9. MAT-V composition and experiment parameters are indicated. **b** and **c**) Comparison of model surface slope distributions for EXP 3, 4, 5, 6, 7, 8, and 9 for the entire model (Fig. 4b) and within the fault zone only (Figs. 4c).

der imposed tectonic forces but also how it erodes under water runoff and, finally, how it scales with natural systems (see section 4.1). To mechanically characterize dry granular materials or natural rocks in the brittle domain, key parameters are cohesion and angle of internal friction (e.g., Byerlee, 1978; Krantz, 1991).

The properties of wet granular mixtures are inherently difficult to measure, making strict control over material placement in the test cell and precise quantification of water content essential. We used a laboratory-built direct shear device (Fig. 7) to determine the Mohr-Coulomb failure envelope of MAT-V. We followed a classical approach by conducting successive shear tests under increasing normal loads. Cohesion and angle of

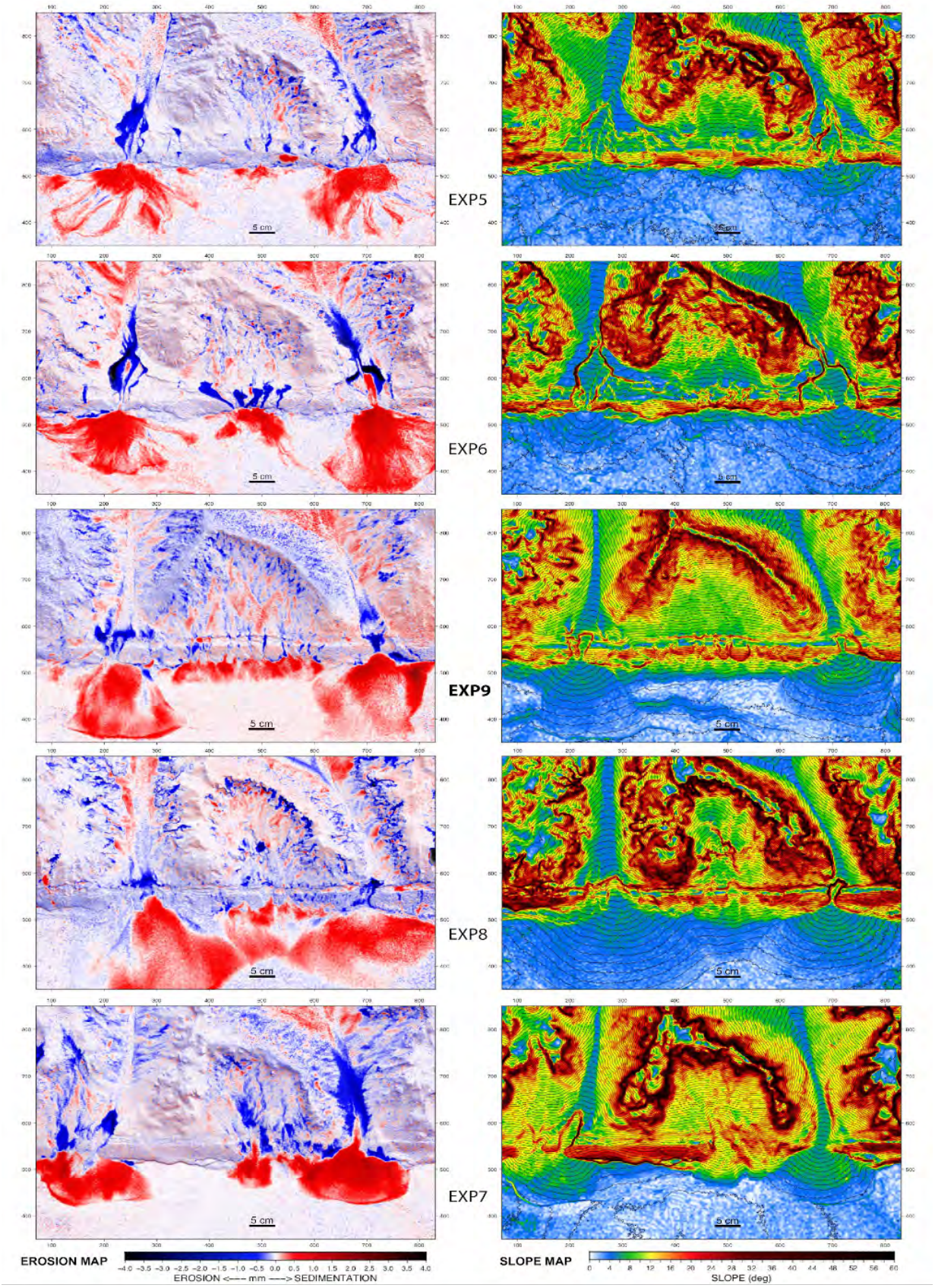

Figure 5 Model erosion (left) and slope (right) maps for different MAT-V compositions. The selected standard MAT-V composition (EXP 9) is centered for easier of comparison.

internal friction measurements were determined for a range of water contents, ranging from 20% to 23% by weight. We focused on this specific range because MAT-V becomes significantly weaker above 23% water and excessively strong below 20%. We also know that when the material is left to rest, its water content stabilizes to about 21-22%. This behavior is systematically observed when freshly mixed material is deposited in the experimental device: it initially flows viscously and solidifies once the excess water has been expelled. Once stabi-

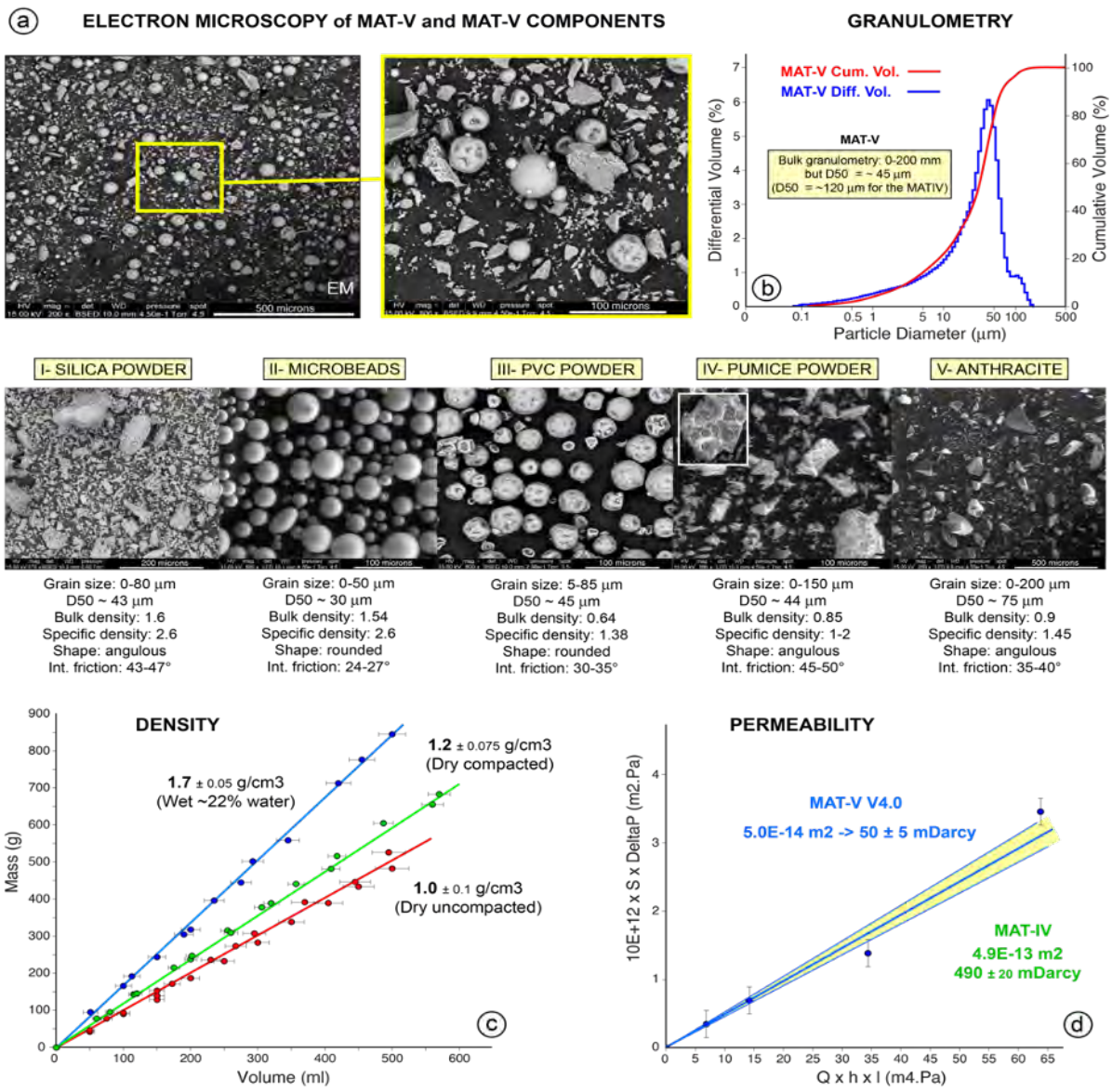

Figure 6 Physical properties of the MAT-V analog material: **a)** Particle shapes, as observed at microscopic scale (SEM). **b)** MAT-V granulometry. **c)** Bulk densities of MAT-V under wet (at 22% by mass of water) and dry (compacted and uncompacted) conditions. **d)** MAT-V permeability measured using Darcy's pipe permeameter.

lized, the material exhibits very low permeability (3.1).

For each measurement, the dry MAT-V mixture is mixed with the targeted water content plus an additional 0.5%. The sample is placed in the test cell and left to rest for 20 to 30 minutes. During this phase, the excess water is collected from the top and through a drainage system at the bottom of the test cell. It is weighed using a ±0.1 g precision scale, to calculate the water content of the sample just before the shear test. Over 35 measurements were performed using this protocol. To complete the shear test measurements, we used a lab-made micro-penetrometer (Fig. 8) to characterize the rheology of the thin layer (critical zone) at the model surface where the MAT-V becomes water saturated due to water run-off. In this state, the material loses its cohesion and transitions from a solid state to a fluidized one, enabling particle erosion and transport.

Due to the difficulty of accurately measuring the water content of each tested sample, the results are subject to some uncertainty. Water content in the material is estimated to be known within ±0.25%. However, reliable failure envelopes can be derived from the Mohr-Coulomb diagram (Fig. 7). Between just over 20% and around 22.5% water content, MAT-V cohesion decreases significantly from approximately 2000 Pa to 200 Pa, respectively. Over the same range, its internal angle of friction appears to decrease from 24° to 33°. Under experimental conditions involving active water run-off, MAT-V water content stabilizes to about 22%, and its bulk cohesion and angle of internal friction can be estimated to ~600 Pa, and ~30° respectively.

Micro-penetrometer measurements (Fig. 8) show that the MAT-V cohesion drops dramatically in the top mm, reaching only a few tens of Pa for water contents between 23–25%. This explains the high sensitivity of MAT-V to surface water run-off: water saturation is rapidly reached, and mechanical erosion is triggered, even by very small drainage or on low slopes.

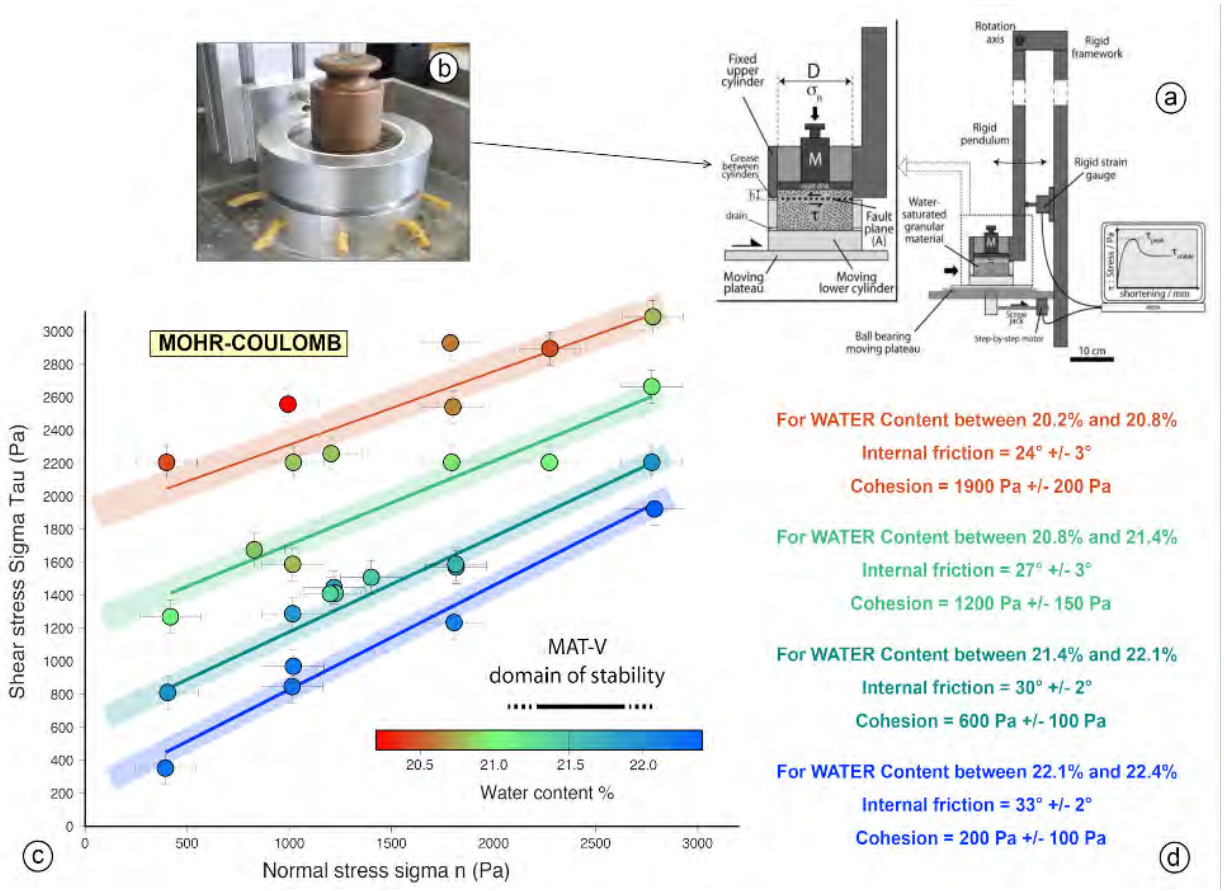

Figure 7 MAT-V mechanical properties. MAT-V cohesion and angle of internal friction were determined from direct shear test measurements, conducted at water contents ranging from 20.2% to 22.4%. MAT-V cohesion decreases by approximately an order of magnitude between ~20% to 22.5% water content. **a)** Principle of the direct shear apparatus. **b)** Photo of the test cell showing the drains. **c)** Mohr-Coulomb failure envelope diagram. **d)** Estimation of MAT-V mechanical properties vs water content.

2.3 Characterization of MAT-V geomorphic properties

2.3.1 Experimental protocol

To characterize the geomorphic properties of MAT-V, we conducted dedicated experiments following the method proposed by Graveleau et al. (2011). The protocol involved a 35 x 35 x 5 cm^3 PVC box filled with MAT-V and precisely tilted to an angle (Fig. 9a). As detailed in section 2.1, the rainfall system delivered water micro-droplets for 5 seconds every 12.5 seconds, resulting in an average precipitation rate of 7.6 mm/h (Table 1). Above the box, the photographic system described in section 2.1 captured images every 30 seconds (Fig. 9b) to monitor topography evolution and generate stereophotogrammetric DEMs at the beginning and end of each experiments. Underneath the box, two tanks collected water and eroded material. The first tank, filled with the incoming water and sediment, had a constant volume maintained using an overflow device. As the eroded material settled at the bottom of the first tank, displaced water flowed into the second tank. Both tanks were weighed every minute using high-precision scales (±0.1 g). The first mass balance tracked the cumulative mass of eroded and transported sediment out of the erosion box, while the second monitored the amount of water delivered by the rainfall system and released during MAT-V erosion. Assuming a water-saturated material density of 1.7 g/cm^3, these mass measurements were converted into a curve representing the cumulative volume of eroded material. The time derivative of this curve provided an estimate of the instantaneous erosion rate across the entire box surface (Fig. 9c). All experiments were conducted following an identical procedure:

- The material was saturated with water and then poured into the box. Excess material was delicately scraped off and leveled with a ruler.
- The material was left to settle overnight to allow partial evaporation of water, allowing the water content of the material to stabilize.
- At the beginning of the experiment, the erosion box was tilted by a fixed angle, and rainfall precipitation was initiated.

During each experiment, we initiated a 30–35 minute calibration of the rainfall system, involving measuring the amount of water delivered every 5 minutes, averaging the mass, and converting it into a rainfall rate (see Table 1). After calibration, we reset both scales. Depending on the tilt angle, the experiments lasted between 0.9 and 5.4 hours (Table 1). In all experiments, the erosion rate was initially high, then decreased and stabilized after about 30 minutes. To account for these variations, we calculated both the mean erosion rate

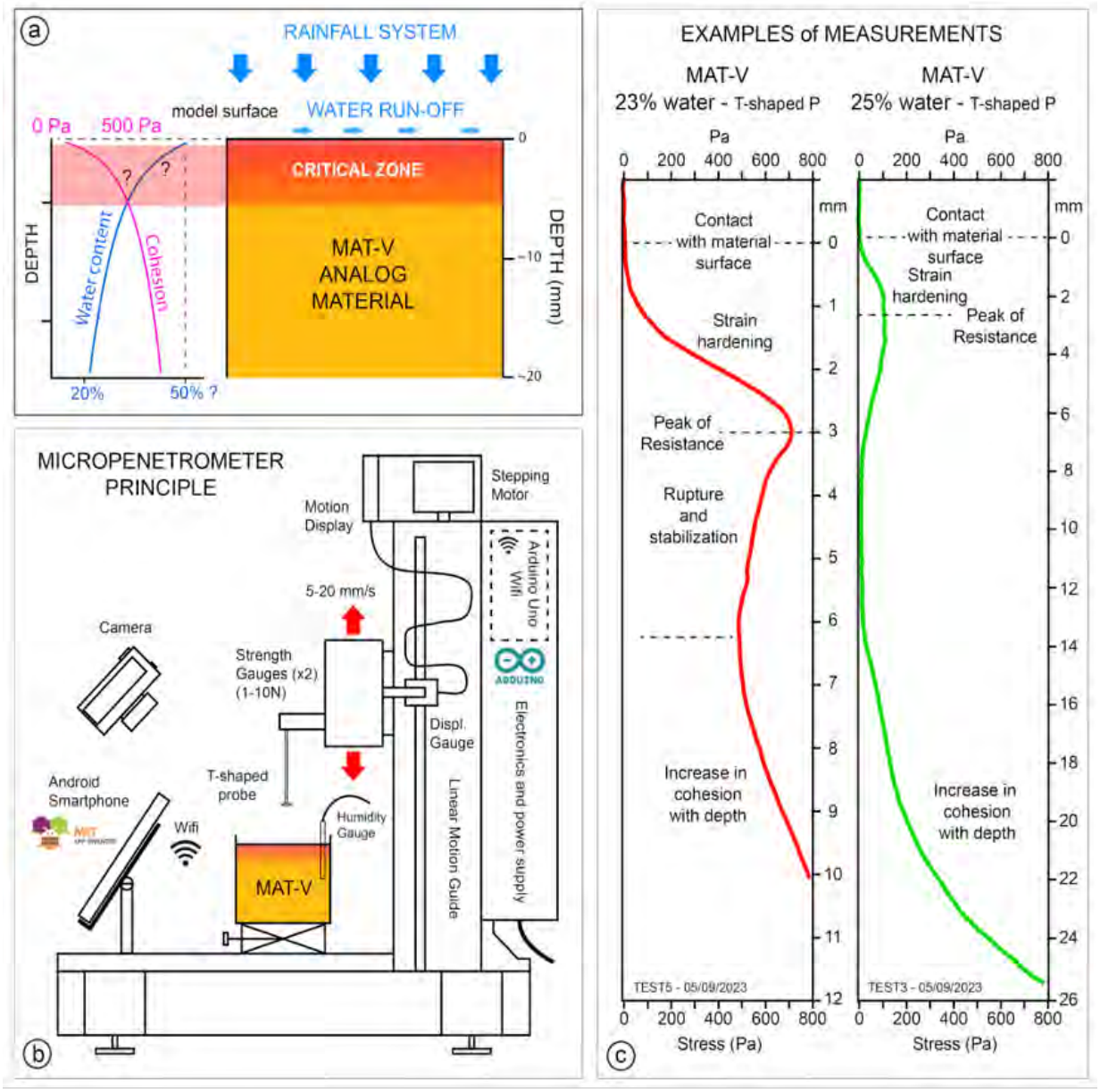

Figure 8 Micro-penetrometer. **a)** Water runoff saturates the MAT-V within the first millimeter of depth (critical zone). **b)** Principle of the experimental device. **c)** Example measurements for two MAT-V samples with high water content (23% and 25%).

over the entire duration of the experiment and a steady-state erosion rate during the phase when the accumulated mass of eroded sediment increased linearly (Fig. 9c).

2.3.2 Erosional properties

The erosion–slope relationship was analysed using 17 experiments. By tilting the erosion box, we varied the initial surface slope a between 2.6–21.3° (see Table 1). The experimental results are in agreement with natural observations (e.g., Roering et al., 1999; Montgomery and Brandon, 2002), which show a linear erosion-slope relationship at low slope (<10°) and a non-linear erosion increase as the slope approaches a critical value (Fig. 10).

Compared to MAT-IV erodibility, measured using the same protocol (Graveleau et al., 2011), the MAT-V erodes at a rate three to four times higher for the same surface slope (Fig. 10). This substantial increase in erodibility was one of the key objectives in upgrading the MAT-IV. Notably, this result was achieved using a much lower rainfall rate (~7 mm/h) compared to that used for MAT-IV (~25 mm/h). This improvement also impacts water run-off on the model surface by reducing water flows, which is crucial for hydrodynamic scaling. Additionally, our results highlight another significant difference between MAT-IV and MAT-V regarding the slope threshold marking the erosion/deposition transition: about 5–6° for MAT-IV and about 2–3° for MAT-V. This value aligns more closely with natural datasets acquired in active mountain ranges (e.g., Montgomery and Brandon, 2002). Finally, both MAT-IV and MAT-V materials start triggering episodic mass-wasting processes for slopes greater than ~15° and ~13°, respectively. Such erosional processes become dominant on slopes steeper than ~20° in MAT-IV and ~17° in MAT-V.

Table 1 Variation of erosion rate associated with erosion-box experiments tilted between 2.6° and 21.8°. The slope refers to the mean surface slope of the model. The experiments involved cyclic rainfall applied during alternating wet and dry periods. Here, only the average rainfall rate and the cumulative eroded volume over the total duration of experiments are indicated. The mean and steady erosion rates refer to the average rates estimated throughout the experiment and at the end of the experiment, respectively.

Model Ref. Name/Date (Day/Month/Year)	Box tilt (°)	Initial slope (± 0.1°)	Final slope (± 0.1°)	Duration (± 0.1h)	Rainfall rate (mm/h)	Eroded volume (cm^3)	Mean erosion rate (mm/h)	Steady erosion rate (± 0.1 mm/h)
EXP7a-2.6d 7/12/2021	2.6	2.6	2.7	5.4	8.1 ± 0.1	58 ± 20	0.47 ± 0.2	0.06
EXP6a-3.3d 20/11/2021	3.3	3.1	3.2	3.2	8.0 ± 0.1	72 ± 20	0.59 ± 0.2	0.1
EXP9a-4d 04/01/2022	4	3.9	4.1	1.3	7.6 ± 0.2	63 ± 20	0.51 ± 0.2	0.25
EXP5a-5d 23/11/2021	5	4.9	4.9	3	8.7 ± 0.1	160 ± 25	1.31 ± 0.2	0.19
EXP10a-6d 11/01/2022	6	5.4	5.8	1.3	7.6 ± 0.2	125 ± 25	1.02 ± 0.2	0.25
EXP4a-7d 18/11/2021	7	7.2	7.2	2.3	7.7 ± 0.1	220 ± 30	1.80 ± 0.15	0.34
EXP11a-8.6d 18/01/2022	8.6	8.4	8.3	1.1	7.2 ± 0.2	154 ± 30	1.26 ± 0.15	0.63
EXP3b-10d 16/11/2021	10	10.1	9.7	1.8	7.8 ± 0.1	311 ± 30	2.54 ± 0.15	1.1
EXP11b-11.2d 18/01/2022	11.2	11.3	10.5	1.2	7.2 ± 0.2	287 ± 30	2.34 ± 0.1	1.46
EXP4b-12.5d 18/11/2021	12.5	12.6	11.3	2.3	7.8 ± 0.1	683 ± 30	5.58 ± 0.1	1.6
EXP8-13.5d 14/12/2021	13.5	13	9.6	2.6	7.8 ± 0.1	1202 ± 20	3.87 ± 0.1	2.04
EXP3b-15d 16/11/2021	15	14.2	13.1	1.4	7.5 ± 0.2	747 ± 30	6.10 ± 0.1	2.05
EXP10b-16d 11/01/2022	16	15.7	14	1.8	6.9 ± 0.2	1166 ± 30	9.51 ± 0.1	1.8
EXP13-17d 01/02/2022	17	17	14.5	0.9	7.6 ± 0.1	521 ± 30	4.25 ± 0.1	5.75
EXP12-18d 01/02/2022	18	17.7	17.1	1.2	7.3 ± 0.2	1003 ± 30	8.19 ± 0.1	4.86
EXP5b-20d 23/11/2021	20	18.2	19.4	1.5	7.8 ± 0.2	1324 ± 30	10.81 ± 0.1	2.36
EXP14-21.8d 08/02/2022	21.8	21.3	31.3	0.9	7.0 ± 0.2	790 ± 25	6.45 ± 0.1	9.19

2.4 Combined experimental-numerical approach

In the previous section, MAT-V was shown to accurately simulate the main surface processes. To further compare the dynamics of erosion, sediment transport, and deposition in MAT-V models with those observed in nature, we developed a joint modeling approach combining experimental and numerical modeling.

2.4.1 Numerical modeling procedure

For numerical landscape modeling, we used the Landlab software (Hobley et al., 2017; Barnhart et al., 2020), a Python-based modeling environment. We used a length-scaling ratio of 10^{-4} (1 cm in the model represents 100 m in nature) and a time-scaling ratio of 10^{-8} (1 s represented 3 years), (see discussion on the model scaling in section 4.1). The numerical modeling was conducted on a 3.5 x 3.5 km^2 area, meshed with a resolution dx of 35 m, over time spans ranging from 9,720–58,320 years using a time step of 5 years, aligning with the 17 experimental models. The initial topography of the numerical model was based on DEMs measured at the beginning of the analog experiments. We set the model's top, right, and left edges as closed boundaries. As in the experimental model, we imposed cyclic climatic forcing with alternating dry and wet periods of 35 and 15 years, resulting in an average precipitation rate of 0.3 m/yr.

We considered two erosion laws to simulate surface dynamics related to erosion, transport, and deposition (Barnhart et al., 2019). Fluvial processes were modeled using a mass balance approach that accounts for the total sediment mass in the channel bed and its transport. This approach was coupled with an explicit representation of the sediment transport length scale, allowing us to derive a range of erosional and depositional responses in river channels (Davy and Lague, 2009). The topographic evolution, $\partial z/\partial t$, depends on the water and

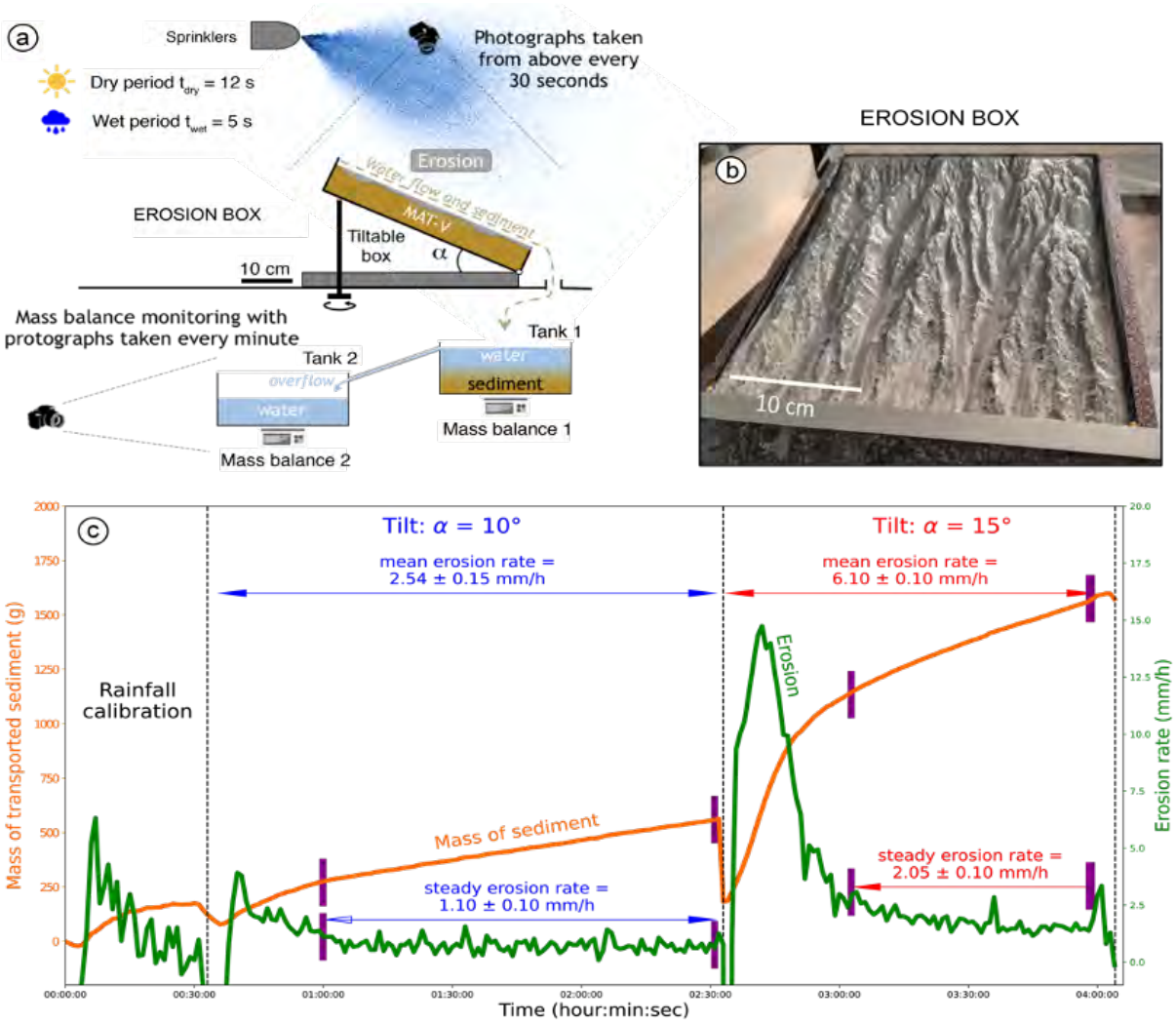

Figure 9 Erosion-box experiment. **a)** Experimental set-up is a tilted box filled with MAT-V, a four sprinklers rainfall system, and two collector tanks. The mass of the tanks is recorded every minute to monitor water and sediment discharge. Cyclic rainfall is applied, alternating between dry and wet periods of 12.5 and 5 seconds, respectively. Photographs are captured every 30 seconds to document changes in surface morphology. **b)** Photograph showing the erosion box for a 15° tilted experiment after 1.4 hours. **c)** Example of erosion rates assessment (green line) based on cumulative sediment mass measurements (orange line). Two successive experiments were conducted at tilt angles of 10° and 15°. A calibration phase quantifies the mass of water delivered to the box surface. The mean erosion rate is determined from the cumulative eroded mass over the full experiment duration. The steady erosion rate is calculated considering the part of the experiment where the accumulated mass of eroded sediment increases linearly.

sediment discharges q and q_s, and the topographic slope S, given by Equation 1:

$$\left(\frac{\partial z}{\partial t}\right)_{river} = V_s \times q_s/q - kq^m S^n \quad (1)$$

where V_s is an effective settling velocity, k is a substrate erodibility, n and m are slope and discharge exponents (Table S1). We assumed no critical stream power to erode the river substrate in our computation (see 4.3). Following the same approach, we also considered a hillslope diffusion law controlled by sediment discharge and local topographic slope (Carretier et al., 2016):

$$\left(\frac{\partial z}{\partial t}\right)_{hillslope} = q_s \times (1-(S/S_c)^2)/dx - \kappa_{hill} S \quad (2)$$

where κ_{hill} is a hillslope erodibility, and S_c is a critical slope controlling landslide and mass wasting events.

Assessing erosion law parameters such as V_s, k, n, m, κ_{hill}, and S_c from natural landscapes requires testing a wide range of values for these erosion law parameters (Table S1). To calibrate these parameters for MAT-V, we used a stochastic approach, comparing outcomes from both experimental and numerical models. This approach is challenging because if two models display similar morphological patterns but have slightly shifted drainage networks, a direct comparison of their final topographies may incorrectly suggest that they are morphologically different. To address this issue, we defined three dimensionless parameters – slope distribution, drainage density, and erosion rate – to compare results from both approaches. The slope distribution was estimated from the detrended surface topography by subtracting the final topography from the initial topography. We assumed a log-normal distribution with a mean, μ, and standard deviation, σ, for which the density function of slopes pdf is given by Equation 3:

$$pdf = 1/(S\sigma\sqrt{2\pi}) \times exp\left(-(lnS-\mu)^2/(2\sigma^2)\right) \quad (3)$$

The slope distribution associated with the experimental and numerical models was then defined by the median $m_{slope} = exp(\mu)$ and the geometric standard deviation $\sigma_{slope} = \sqrt{(exp(\sigma^2)-1)} \times exp(2\mu+\sigma^2)$. We also used the

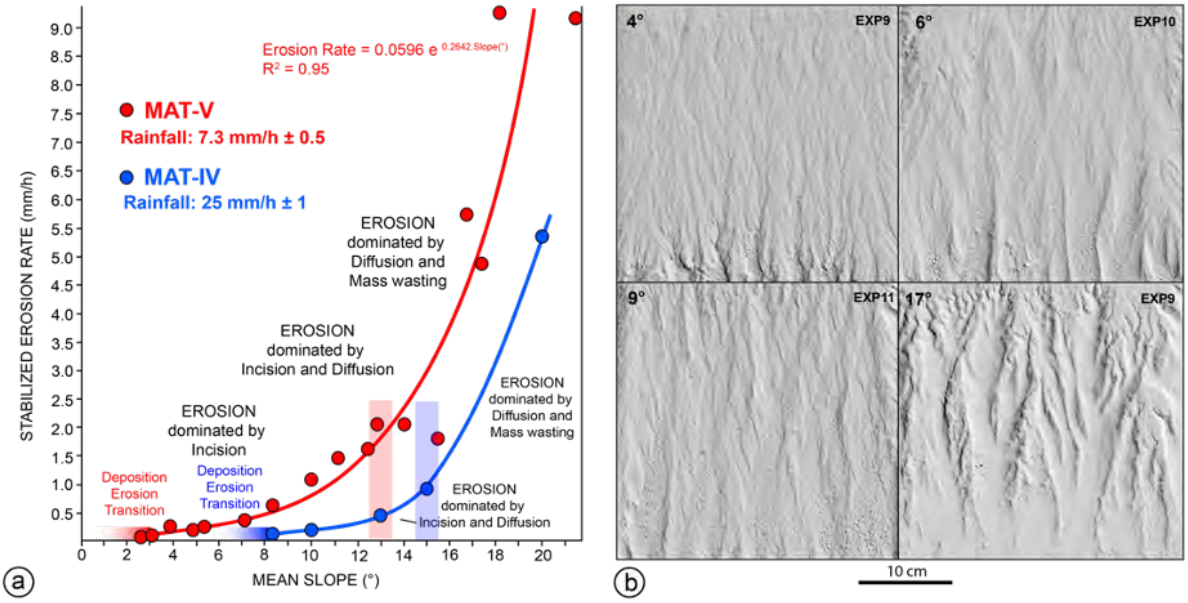

Figure 10 Comparison between MAT-IV and MAT-V erodibility as a function of mean slope. **a)** Stabilized erosion rates versus mean topographic slope. **b)** Examples of erosion box morphologies for different initial slopes (standard MAT-V composition) during steady-state erosion phases.

drainage density function available in Landlab, which calculates the distance from every node to the nearest channel node, L, along the flow line of the steepest descent. The dimensionless drainage density is then calculated (after Tucker et al., 2001):

$$D_d = dx/2\bar{L} \quad (4)$$

where $\bar{L}$ is the mean L for the model domain meshed with a resolution dx. The erosion rate was further processed to ensure comparability. We normalized the erosion to the maximum rate, using the mean erosion rate measured over the total duration of the experiment and the difference between the initial and final topography of the numerical model. Finally, the agreement between experimental and numerical results, $L_{\text{Normalized}}$, was calculated as the product of the normalized likelihoods associated with slope distribution, drainage density, and erosion rate as defined in Equations 5 and 6:

$$L = \prod_{i=1}^{4} L_i/(l^i{}_{\max}) \quad \text{and} \quad L_{\text{Normalized}} = L/L_{\max} \quad (5)$$

where

$$l^i = exp\left(-\sqrt{1/17\sum_{k=1}^{17}(Pexp_k^i - Pnum_k^i)^2}\right) \quad (6)$$

with $Pexp_k$ and $Pnum_k$ were the parameter vectors $[m_{\text{slope}}, \sigma_{\text{slope}}, D_d, Erosion]$ associated with the erosion-box tilt .

Our research involved a significant computational effort, as we stochastically explored 33,928 combinations of geomorphic parameter values within the ranges given in Table S1 and calculated their associated normalized likelihoods. For each model, the 17 tilted experiments were considered, leading to 576,776 simulations. The greater the number of simulations, the better the model space will be explored. Here, the number of simulations performed allows us to define a confidence interval corresponding to approximately 1/6 of the parameter's explored range. We took advantage of the Python multiprocessing module to reduce the computation time, which took approximately two months, on a high-performance workstation equipped with a Intel® Xeon® Gold522OR processor (96 cores).

2.4.2 Hillslope diffusion and river incision properties

The best agreement between the experimental and numerical models (associated with the best likelihood model, i.e $L_{\text{Normalized}}$=1) was obtained for V_s≈10.7 m yr^{-1}, k≈8×10^{-5} m$^{-0.14}$ yr$^{-0.43}$, n≈1.61, m≈0.57, κ_{hill}≈9.6×10^{-4} m yr^{-1}, and S_c≈29.7°. Using these values, the numerical model effectively replicates the main geomorphic features of the experimental model, regardless of the erosion-box tilt and experiment duration (Figs. 11 and 12). For both approaches, the median slope (m_{slope}), geometric standared deviation of the slope distribution (σ_{slope}), and the mean erosion rate increase with the erosion-box tilt while the drainage density remains constant. In addition, despite the exponent n≈1.61, our results suggest a linear relationship between the median slope (m_{slope}) and the erosion rate, highlighting the combined effect of river and hillslope processes. The main discrepancy lies in the river's entrenchment, with channels more deeply incised in the numerical model because lateral erosion processes were not included in the simulation (see 4.2).

In the previous paragraph, we presented the results that best matched the experimental and numerical outcomes. The 33,928 calculated models also allow us to characterize the distribution of erosion law parameters associated with the most likely models and to examine their interdependence. Since the tested combinations

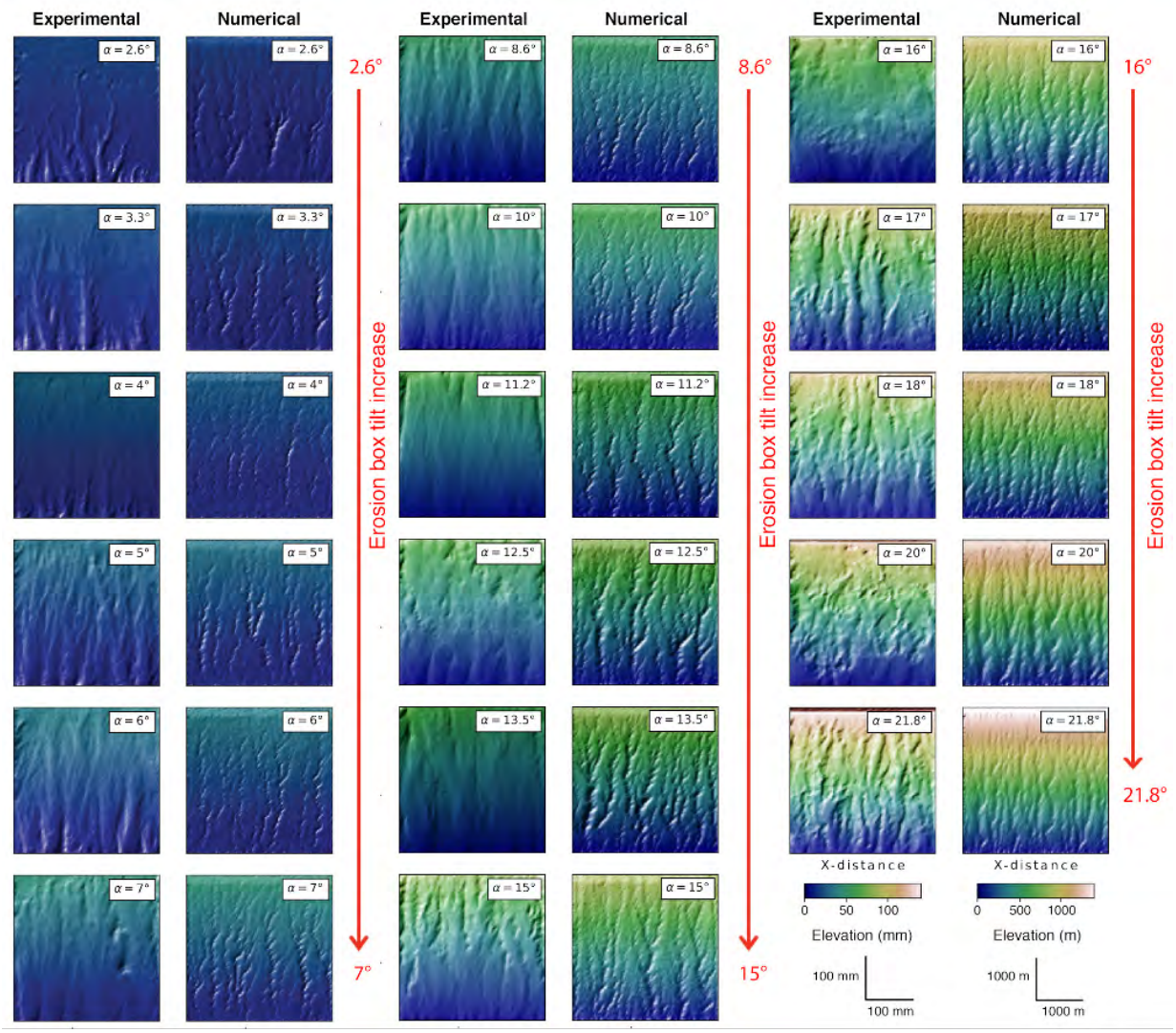

Figure 11 Comparison between the final topographies of experimental and numerical erosion-box models tilted by an angle α between 2.6° and 21.8°. This comparison is based on the best agreement between the experimental and numerical model outcomes, as defined by the slope distribution, drainage density, and erosion rate. Note that different spatial and color scales are used for the two datasets.

were randomly chosen with equal probability, studying the 10% of models with the highest likelihood yields a probability density function (*pdf*) for each model parameter (Fig. 13). The *pdf s* of variables obtained for the top 5% and 10% best-fit models are similar, showing that our results are robust. Hence, in the following, we focus on their common features and do not discuss their minor differences.

The slope exponent n exhibits a flat distribution and remains poorly constrained in the range between 1 and 3 (Fig. 13). In contrast, our approach provides information for the other parameters. The MAT-V effective settling velocity ranges between 0.1 and 10 m.yr^{-1}, indicating equal contributions from transport and erosion and a hybrid response between detachment-limited and transport-limited behavior (Davy and Lague, 2009). The discharge exponent m has a normal distribution with a mean of 0.5 and a standard deviation of 0.15 (Fig. 13). Our result suggests a fairly flat distribution for the river substrate erodibility with a slight increase for high k. The dependency between k and the discharge exponent explains this result. The units of k depend on m, and a trade-off can be observed between these two parameters with an exponential relationship (Figure S1). Concerning the hillslope processes, our approach provides strong constraints, suggesting a hillslope erodibility κ_{hill} between 10^{-4} m.yr^{-1} and 10^{-2} m.yr^{-1} and a critical slope $S_c \geq 24°$ associated with the MAT-V (Fig. 13). Lastly, except for the trade-off between m and k, our results suggest no interdependency among the other erosion law parameters (Figure S1).

Our combined approach shows that MAT-V is well-suited to replicate the evolution of natural landscapes governed by hillslope and river dynamics. The new material represents a significant enhancement by addressing the main limitations of the MAT-IV, such as low erodibility, high values for erosion/sedimentation transition slope angle, and critical slope. Additionally, our findings indicate that the m/n ratio ranges between 0.14 and 0.65, in agreement with the proposed values inferred in nature of 0.35 to 0.63 (e.g., Whipple and Tucker, 1999; Harel et al., 2016), whereas MAT-IV yielded $m/n \approx 1$ (Graveleau et al., 2011).

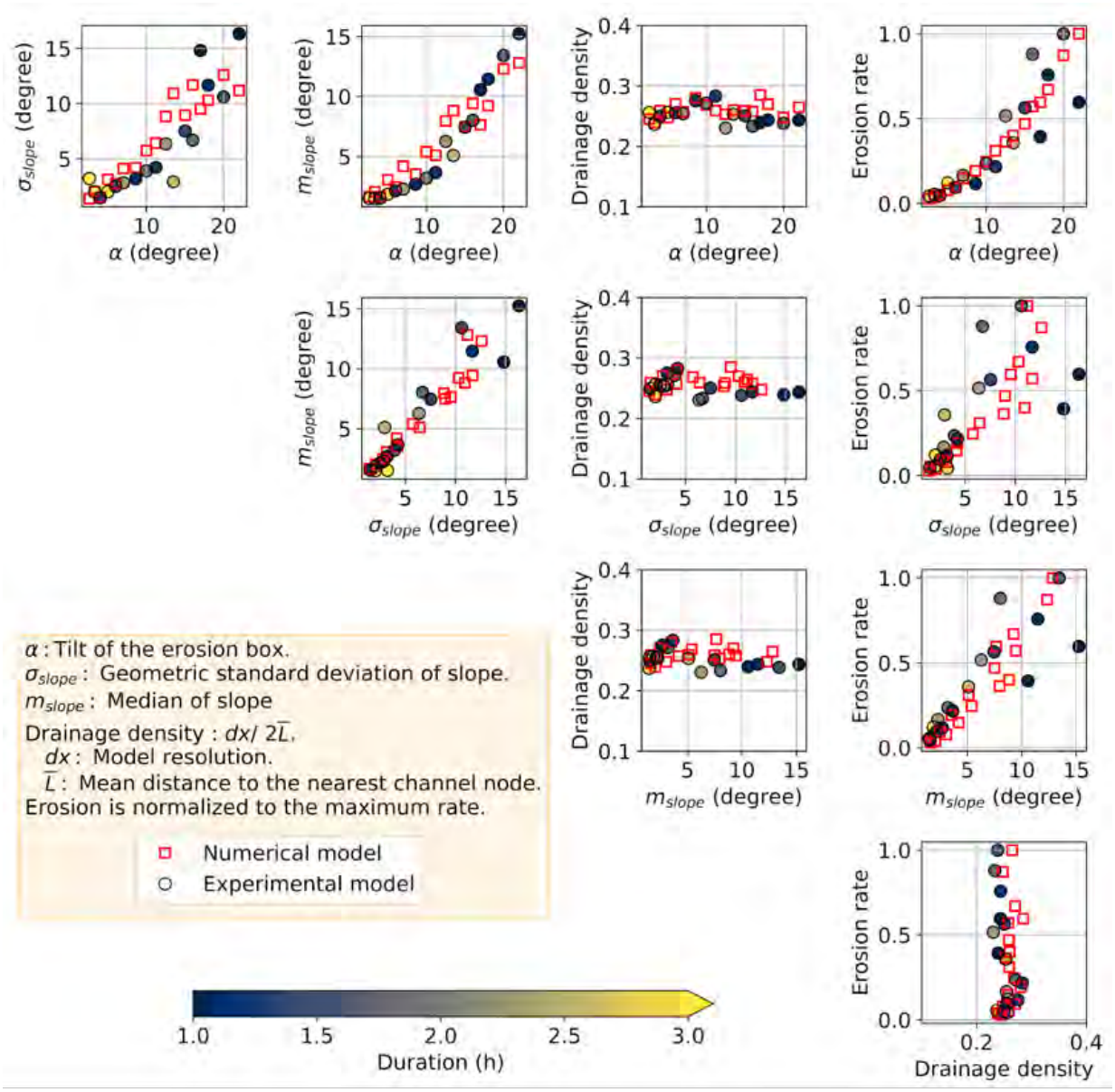

Figure 12 Relationship between geomorphological features characterizing the best agreement between experimental (circles) and numerical (red squares) models. All proxies are dimensionless. The tilt angle of the erosion box is α . The geometric standard deviation and median of the slope change distribution observed at the surface are σ_{slope} and m_{slope}, respectively. Drainage density is estimated at each node based on the mean distance to the nearest channel node (Tucker et al., 2001). Erosion rates are normalized to the maximum observed rate. The color scale indicates the duration of each experiment.

3 Results

The MAT-V analog material displays morphologies and tectonic features that show significant enhancements compared to MAT-IV material.

3.1 MAT-V model geomorphology

As for the MAT-IV analog material (Graveleau et al., 2011, 2012), erosion and transport processes, triggered by water run-off, entail diffusive mechanisms on hillslopes, incision, and lateral erosion in channels. More energetic erosion processes, such as debris flow and landslides, are also observed on steeper slopes (>30°). The combination of these morphogenetic processes generates topography characterized by entrenched valleys separated by ridge divides along with realistic morphological features such as alluvial fans, alluvial and erosional terraces, knickpoints, and more. When using the MAT-V, the local anomalous topographies observed with the MAT-IV, such as overhangs, convex crests, flat-bed channels, and features linked to excessive capillary cohesion and hydraulic forces, are only rarely observed.

3.1.1 Catchments

In nature (e.g., Hovius, 1996), drainage basins in mountain forelands display similar sub-parallel drainage networks, channel patterns (e.g., width vs length ratio), and landforms (e.g., crests) compared to MAT-V based models. This similarity indicates that the erosion and transport processes in the model align with those shaping natural landscapes, i.e., diffusive processes on hillslopes and advective transport in channels. (Fig. 14a).

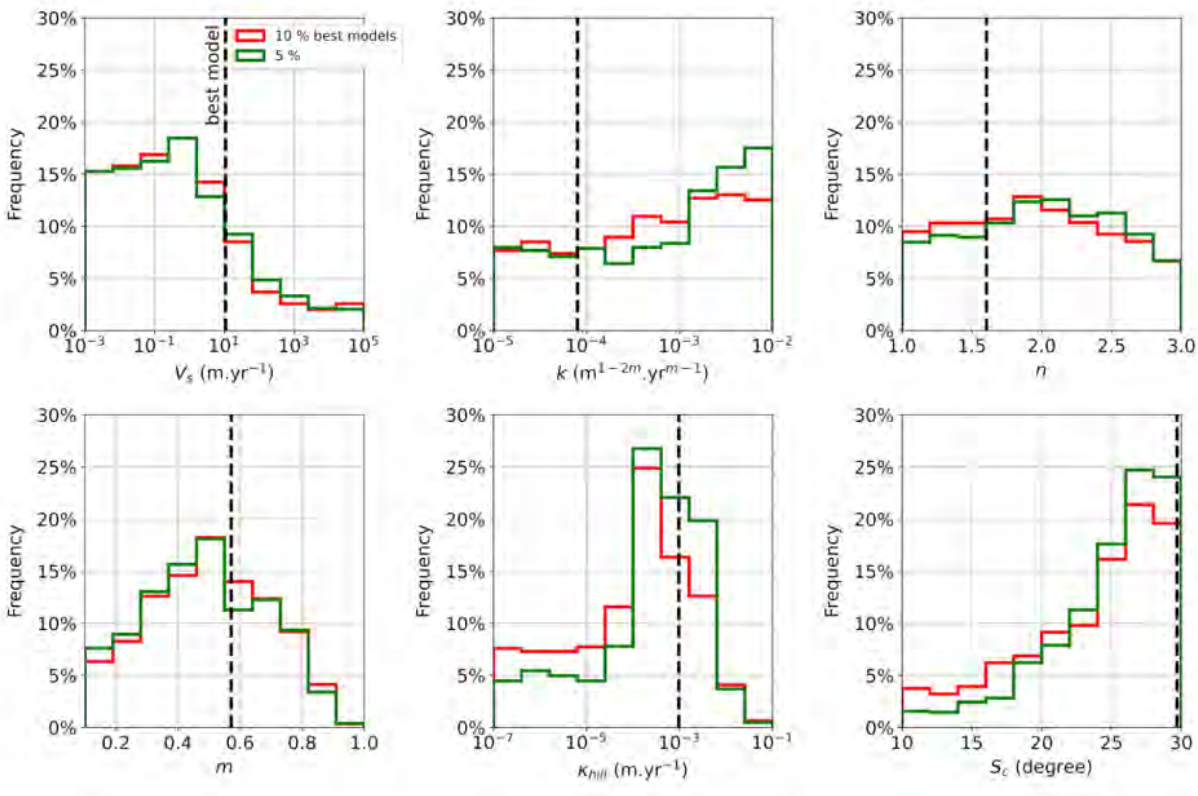

Figure 13 Numerical erosion model parameters and their associated probability density functions, as obtained from the 10% (red line) and 5% (green line) best-fitting models. The vertical dashed line represents the parameter values obtained for the best-fit model (model with $L_{\text{Normalized}} = 1$) out of the 33,928 stochastically explored. Parameters include: V_s: effective settling velocity, k: substrate erodibility, n: slope exponent, m: discharge exponent, κ_{hill}: hillslope erodibility, and S_c: critical slope.

3.1.2 Drainage network

The drainage network displays a dense and arborescent geometry that compares well to natural hydrographic systems when assessed using standard topological and geometric metrics (e.g., stream order and frequency, drainage density) (Fig. 14b). Natural hydrodynamic phenomena such as antecedence, superimposition, stream piracy, and headcut erosion are also observed in the model.

3.1.3 Alluvial fans

Several fan-shaped sedimentary bodies form at the outlets of drainage basins along the deformation front (Fig. 14c). They develop in response to the break in slope and drop in the transport capacity of channels that suddenly widen when reaching the foreland basin. As in nature, their fan shape is controlled by the sweeping and divagation of distributary channels on their surfaces. The experimental alluvial fan slopes (1–5°) fall within the range of values measured in mountain forelands (e.g., Blair and McPherson, 2009).

3.1.4 Alluvial surfaces

Both channel and alluvial fan dynamics lead to the coexistence of preserved alluvial surfaces intersected by active channels (Fig. 14c). In the model, these alluvial surfaces range from a few cm^2 up to a few hundred cm^2, and their thicknesses generally do not exceed a few mm (equivalent in nature to approximately 0.05–5 km^2 and <100 m, respectively).

3.1.5 Knickpoint

Knickpoints, about 1–2 mm in amplitude (equivalent to 10–20 m in nature), are observed along the main channels. These features form in response to channel incision and upstream erosion driven by internal catchment uplift and tectonically controlled base-level changes. Knickpoints originate near the active fault zone and migrate upstream at rates that gradually decrease from a few centimeter per hours to a few millimeters per hour (equivalent to 1 cm to 1 mm per year in natural settings). This retreat velocity lies in the lower end of the spectrum compared to those observed in rapidly uplifting or actively eroding landscapes (e.g., Crosby and Whipple, 2006; Whittaker and Boulton, 2012).

3.1.6 Fluvial terraces

Sets of stair-step surfaces are often observed where channels cross active faults but also in the internal parts of drainage basins (Fig. 14c). These surfaces form in response to localized tectonic surface deformation such as faulting, folding, and to drainage network dynamics, such as channel divagation, stream piracy, river bed incision, that entail variations in hydraulic flows. Elevation differences between these surfaces vary from 1 to a few mm. (i.e., 10–50 m in nature). The amplitude and morphology of these stair-step surfaces compare well

with uplifted fluvial terraces in active mountain foreland settings (e.g., Charreau et al., 2018).

3.1.7 Lake

Long-lasting or temporary lakes, along with associated specific deposits (prograding sedimentary bodies, paleo shorelines) can also be observed. Lakes develop primarily in the foreland basin, but also occur in regions with more contrasting topography, such as piggyback basins. Occasionally, lake-drying episodes occur in response to channel network reorganization or surface deformation triggered by nearby tectonic activity.

3.2 MAT-V Deformation mechanisms and tectonic styles

The MAT-V material develops a wide range of morphotectonic structures depending on the studied geological context and imposed boundary conditions. Under a compressive tectonic regime, equivalent to horizontal crustal shortening, MAT-V deforms through the development of reverse faults and low-angle thrusts, often associated with steeper conjugated back-thrusts. Extrados deformation, expressed by steep, low amplitude, normal faults network, also develops in response to generalized folding caused by tectonic compression or to localized folding associated with variations in fault plane geometry.

3.2.1 Fault zone deformation

Major reverse faults appear associated with a zone of distributed deformation extending along their surface trace (Fig. 15a). Including folding, these zones can extend up to several tens of centimeters (equivalent to several kilometers in nature). Different types of faults can be observed: thrusts, conjugated reverse faults, and extrados normal faults. Not all of these faults are preserved over a long period, and the processes of erosion and sedimentation can mask or erase them in whole or in part.

3.2.2 Internal model structure

Cross-sections, performed at the end of the experiment, reveal the model's internal deformation and illustrate how interactions between tectonics and surface process are recorded in the sedimentation (Fig. 15b). Distinct units, differentiated by color (white, gray, or black) can be identified. These are gently folded upstream and offset by the main reverse fault (thrust). In most sections, secondary faults can also be observed, including extrados faulting and conjugated low dipping reverse faults. The ante-tectonic layers, deposited in a coarse, unorganized manner before the experiment, appear as homogeneous gray units, textured by anthracite grains, whereas syntectonic deposits appear lighter and display clear stratification. Using heterogeneous grains in the MAT-V formula (varying in size, shape, and density) favors particle sorting during transport and deposition. Sorting occurs both vertically (lamination) and horizontally (proximal to distal facies changes). This syntectonic stratification underlines key sedimentary structures, such as cut-off and downlap, which can be investigated to gain insights into the evolution of sedimentary rates, tectonic activity, and erosive phases, as previously demonstrated by Viaplana-Muzas et al. (2015, 2018) using MAT-IV.

3.2.3 Morphological expression of the fault trace

The surface expression of faults, and other tectonic features, depends on local erosion and sedimentation conditions (Fig. 15c). At the deformation front, the fault trace propagates through active alluvial fans, interacting with these highly dynamic geomorphic features. As observed in natural settings, the fault trace is barely discernible within the main active drains meandering across the fan surface, except during a short period following an incremental slip event (ie., an earthquake).

The co-seismic surface rupture is rapidly erased, within a few seconds of experimental time, equivalent to a few years or decades. In less active regions of the alluvial fans, a cumulative fault scarp, several millimeters high (equivalent to tens of meters in nature), forms over time. As in natural settings, its topographic expression is most pronounced on uplifted alluvial and fluvial terraces. Their flat topographies combined with their isolation from the active drainage network constitute optimal conditions for fault scarp preservation.

4 Discussion

Analog modeling of landscape evolution provides a unique tool for investigating the complex interactions between endogenic forces (tectonic and volcanic) and exogenic processes (erosion and sedimentation). When analogous processes and scalings are achieved, this approach represents the most advanced methodology currently available for the simultaneous simulation of complex three-dimensional geomorphic systems. Because analog modeling can handle across both short and long temporal and spatial scales, it opens the way to a better understanding of how landscapes evolve and respond to tectonic and climatic forcings. The relevance of the experimental approach is strongly dependent on the properties of the analog material, the imposed boundary conditions, and the model monitoring techniques, and can be further enhanced by integrating it with numerical modeling.

MAT-V represents a significant upgrade of the earlier MAT-IV analog material developed to for investigating relief dynamics in active tectonic settings. Its improved geomorphological properties and rheological characterization open new fields of application for the study of landform dynamics. To support future studies research using MAT-V, we address key issues related to model scaling, as well as the strengths and inherent limitations of the material.

4.1 Scaling

The primary objective of analog modeling is to study geological processes at reduced spatial and temporal

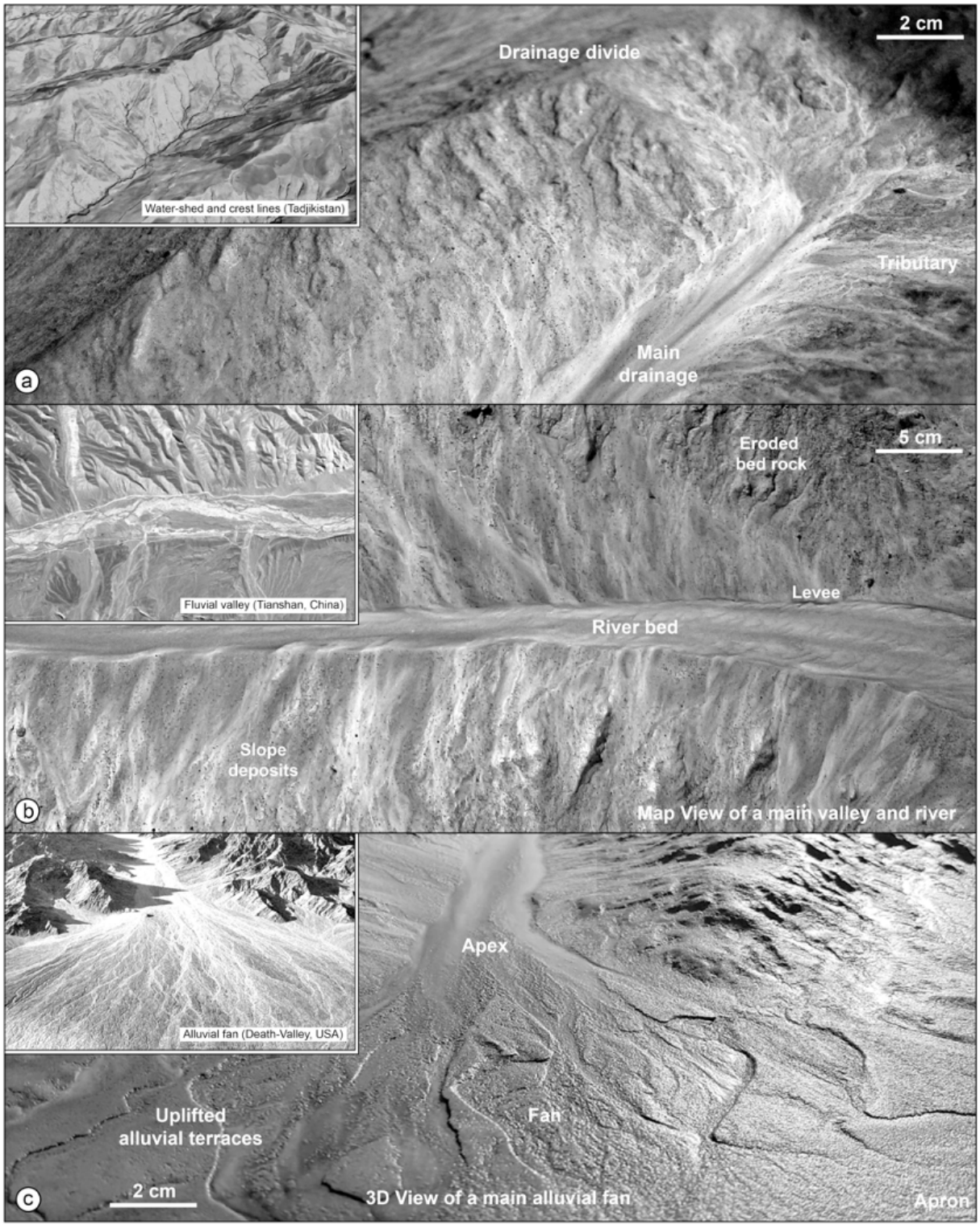

Figure 14 Selection of experimental morphologies obtained with the MAT-V standard composition. **a)** 3D view of the upper portion of a main watershed showing crest lines and drainage divide morphologies. **b)** Map view of a main channel situated in the lower portion of a large catchment. Note the diversity of sedimentary bodies distributed along the channel. **c)** 3D view of a large alluvial fan developing at the front of the relief area, and spreading over the foreland basin. Several alluvial surfaces of different abandonment ages can be observed.

scales. To achieve this goal, scaling relationships are essential for defining model parameters and extrapolating modeling results to natural systems. In most published studies on tectonic analog experiments (e.g., Davy and Cobbold, 1991; Mugnier et al., 1997; Graveleau et al., 2015; Schellart and Strak, 2016; Reber et al., 2020), the approach to constrain scaling follows a general methodology first established by Hubbert (1937) and later refined by Ramberg (1981). These scaling rules, derived from similarity theory and the fundamental equation of dynamics for continuum medium in non-dimensional form, are applied to define the model's geometric, kinematic, mechanical properties, and boundary conditions. When properly applied, these rules ensure that the model will reproduce, to a meaningful extent, the dynamic behavior of the targeted geolog-

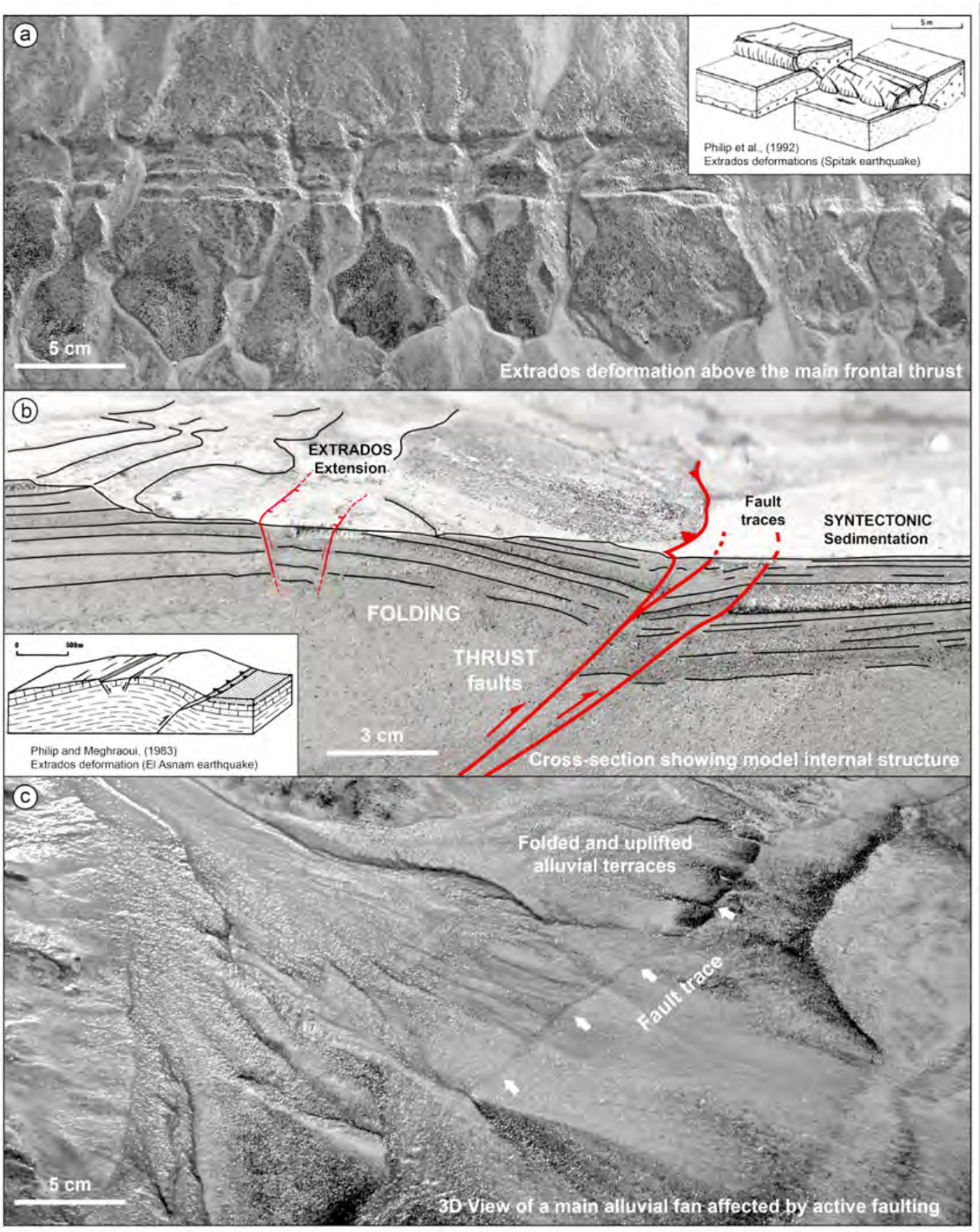

Figure 15 Examples of tectonic structures and related morphologies developing during experiments using the standard MAT-V composition. **a)** Extensive extrados deformation induced by reverse faulting and folding, compared to the El Asnam seismogenic fault surface morphology (Philip and Meghraoui, 1983). **b)** Cross-section, performed at the end of the experiment, showing the interactions between reverse faulting and syn-tectonic sedimentation. **c)** Side view of a large alluvial fan crossing the thrust front, showing the morphological relationship between the fault trace generated by the last fault slip event and the cumulative fault scarp, along with active and abandoned alluvial surfaces.

ical process (e.g., Paola et al., 2009; Weijermars and Schmeling, 1986; Reber et al., 2020). In practice, however, rigorous scaling is rarely achieved for several reasons. First, key parameters, controlling both natural and model rheologies are often constrained with significant uncertainties. Second, our understanding of the physical laws that govern natural processes remains incomplete. Third, geological processes operate over a wide range of spatial and temporal scales, each with distinct response times, making it virtually impossible to replicate them all simultaneously in a single experiment. Nonetheless, recent advances in analog tectonic modeling (e.g., Caniven et al., 2015; Rosenau et al., 2017), have demonstrated that reliable model scalings

can be achieved. This raises the question: Can geomorphic analog models be scaled with similar rigor? And specifically, how should MAT-V-based analog models be scaled to accurately simulate landscape evolution processes?

4.1.1 Spatial, mechanical and temporal scaling

The length scaling ratio (L^*), which defines the ratio between a length measured on the model and the corresponding distance in nature, is generally to be determined first. Analog experiments investigate natural processes and geological structures with characteristic spatial dimensions ranging from several hundred meters to hundreds of kilometers. Because experimental devices are hosted in laboratories and rarely exceed a few meters in length, L^* is typically confined to a narrow range. In classical sandbox experiments investigating mountain building processes, the L^* commonly ranges between 10^{-5} and 10^{-6}, meaning that 1 cm in the model corresponds to 1-10 km in nature. This scaling makes it possible to model a portion of the crust, several hundred kilometers long within a 1 to 2 m long experimental set-up (e.g., Davy and Cobbold, 1991; Konstantinovskaia and Malavieille, 2005, see Schellart and Strak (2016) for a review). In contrast, geomorphic experiments focus on smaller-scale natural features, with characteristic lengths typically ranging from tens of meters to a few kilometers. As a result, L^* usually falls between 10^{-3} and 10^{-5} (1 cm in the model corresponds to 10–1000 m in nature). As detailed below, MAT-V was designed to target a spatial scaling ratio of 1–2x10^{-4} (1 cm = 50–100 m), enabling the modeling a 5–10 km wide landscape on a 1-m long experimental device.

To constrain the rheology of the model and scale its mechanical properties to natural conditions, Hubbert (1937) defined a dimensionless relationship that links the ratio of surface-to-body forces, incorporating the previously defined length scaling factor (L^*): (C^*) = $\rho^*.g^*.L^*$, where C^*, ρ^*, g^* and L^* represent the model-to-nature ratios for cohesion, density, gravity, and length, respectively. Assuming that ρ^* is about 0.75 (wet MAT-V has a density of 1.7 g/cm^3 and consolidated sedimentary rocks, an average density of 2.3 g/cm^3; Grant and West (1965), $g^* = 1$ (experiments are performed in the Earth's gravity field), and L^* = 1.3x10^{-4} in average, led to a C^* of about 10^{-4} (1 MPa in nature corresponds to 100 Pa in the model). To determine appropriate model mechanical properties (specifically, cohesion and angle of internal friction for rocks in the brittle domain), it is essential to identify relevant values for natural rock cohesion. Geomechanical tests on intact consolidated sedimentary rock indicate that cohesion values extend over a range of a few tens of Megapascals (e.g., Krantz, 1991). These cohesion values should not be used without some corrections as bedding planes, fractures, and the presence of weak horizons significantly reduce the effective cohesion of rock masses at length scales exceeding a few tens of meters (Hoek and Brown, 1988, 1997). Therefore, we find it more relevant to consider sedimentary rock cohesion values in the range of 5–15 MPa when calculating the corresponding scaled cohesion for the analog model. Applying the previously calculated cohesion ratio ($C^* = 10^{-4}$) yields an average model cohesion of approximately 750 Pa. Finally, since the angle of internal friction is a dimensionless parameter, scaling rules dictate that it should remain the same in both the model and nature. For sedimentary rocks, this angle typically ranges around 30 ± 5°, (e.g., Byerlee, 1978; Al-Hashemi and Al-Amoudi, 2018). As shown in Fig. 7, the mechanical properties of the MAT-V material satisfy the requirements mentioned above.

Depending on the material water contents (21–22% under the experimental conditions), its cohesion ranges from 500 to 1000 Pa and its angle of internal friction from 24° to 33° (Fig. 7). If a different length scaling ratio (ρ^*) is needed, such as to model a kilometer-scale landform using a 1 cm = 10–20 m spatial scaling, the MAT-V cohesion should be increased to more than 3000 Pa. Conversely, to model a 100 km long mountain front using a 1 cm = 1000 m spatial scaling, the MAT-V cohesion should be reduced to below 100 Pa. Such modifications to MAT-V cohesion could be achieved primarily by modifying the relative proportions of Silica Powder and Microbeads and, if necessary, by adjusting those of the other MAT-V components. However, the cohesion of wet granular materials is inherently constrained by physical laws, and achieving such extreme spatial scaling will inevitably compromise the morphological rendering of the model.

In geomorphic experiments, constraining temporal scaling of the model is often the most challenging aspect. Various semi-empirical methods have been employed to address this issue (e.g., Graveleau, 2008; Graveleau et al., 2012; Reitano et al., 2020, 2022, 2023; Mao et al., 2021; Conrad et al., 2023). To estimate T^*, the ratio between a time interval in the analog model (T_m) and the corresponding time in nature (T_n), we use the following equation:

$$V^* = V_m/V_n = L_m/T_m/L_n/T_n = L^*/T^*$$

where V^* is the model-to-nature velocity ratio, inferred from average erosion and sedimentation rates measured under the imposed tectonic and rainfall conditions.

Using the erosion maps, obtained from precise vertical differencing measurements during the MAT-V testing phase, we quantified minimum and maximum erosion and sedimentation rates of about 1–10 mm/h (Figs. 16a and 16b). In natural mountain foreland settings, they typically range between 1–10 mm/yr (e.g., Jolivet et al., 2014). These values yield a velocity ratio V^* of approximately 10^{-4}. Applying this value, along with the previously defined length scaling factor L^* = 1.3x10^{-4}, results in a time ratio T^* of approximately 10^{-8}, meaning that one second in the model is equivalent to a few years (3–5 yr) in nature.

4.1.2 Fluid dynamics

The Reynolds (Re) and Froude (Fr) numbers are dimensionless parameters used to characterize the contribution of water flows to landscape dynamics and should ideally be similar between the models and natural systems. The Reynolds number describes the ratio of in-

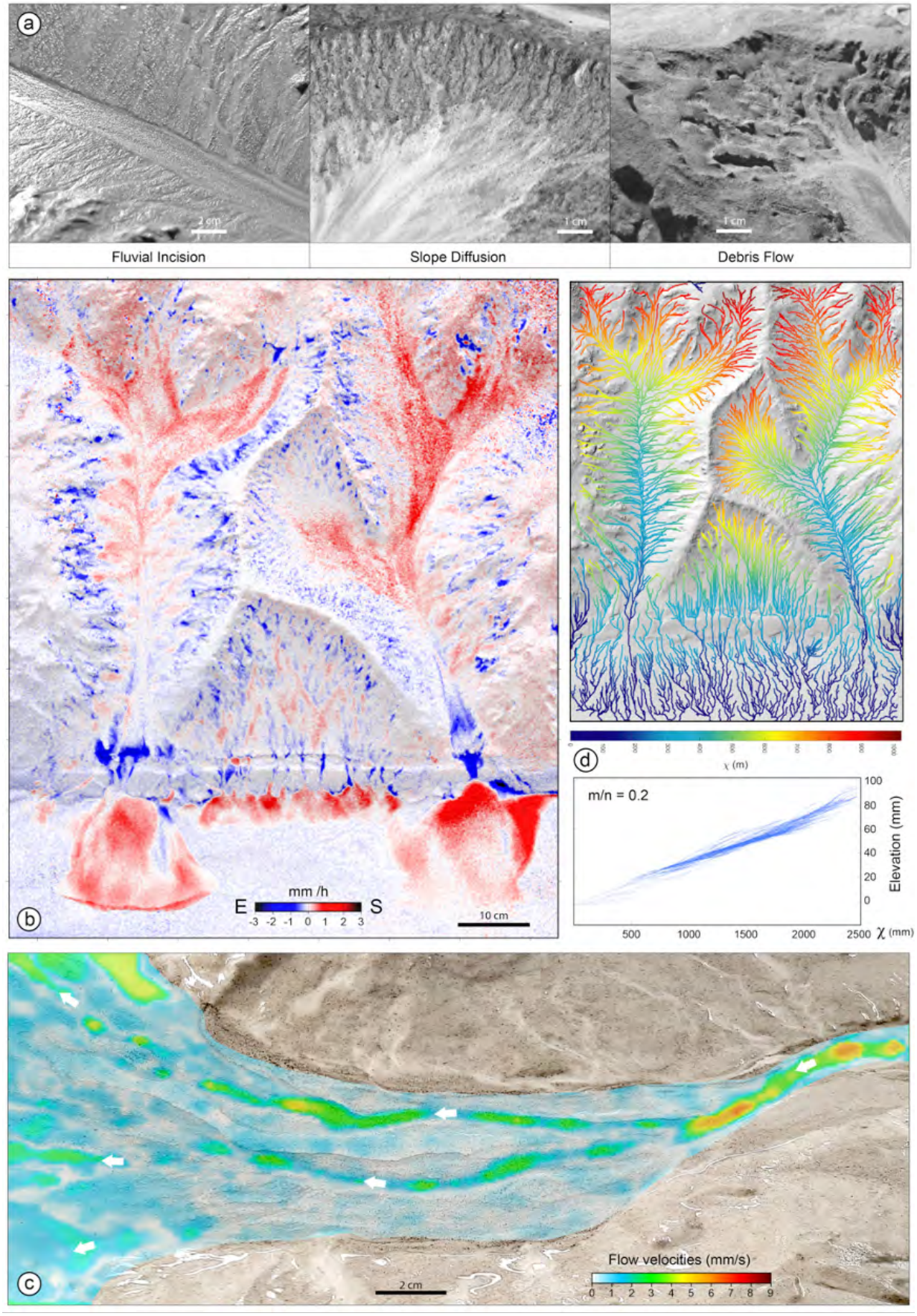

Figure 16 Examples of model monitoring. **a)** Model morphologies illustrating specific morphogenetic processes. **b)** Erosion map used to quantify local and mean erosion and sedimentation rates. **c)** Kinematic analysis (via image correlation) used to quantify sediment transport velocities within active channels. **d)** Morphometric analysis: Chi-map used to investigate watershed interactions and channel morphometric characterizations.

ertial forces to viscous forces while the Froude number represents the ratio of inertial forces to gravitational

forces. In open channels (Chaudhry, 2008), when Re is in the range of 500–2000, the flow regime is considered transitional (inertial forces ~viscous forces), and below 500, laminar. When Re > 5000, the flow is considered turbulent (inertial forces » viscous forces). Similarly, when Fr < 1 (gravity-dominated inertial forces), the regime is sub-critical or fluvial, and when Fr > 1 (Inertial forces dominate gravity), it is super-critical or torrential (Chaudhry, 2008). Previous experimental studies have compared these numbers in models and in natural systems (Lague et al., 2003; Niemann and Hasbargen, 2005; Rohais et al., 2012). In our experiments, based on kinematic and topographic measurements on active channels, water flow velocity, u, is 0.005 to 0.01 m/s and water flow thickness, D, is 0.001 to 0.005 m (Fig. 16c), yielding Re of ~20 and Fr of ~0.04 (using a kinematic water viscosity of 10^{-6} m^2/s at 20°C). These results show, firstly, that while Froude numbers are broadly comparable between the model and natural rivers (Fr < 1), this is not the case for Reynolds numbers. Experimental Reynolds numbers consistently indicate laminar regimes, while their natural counterparts correspond to turbulent regimes (Re > 10000). This is all the more true at small scales, where water viscosity (and thus viscous forces) is greatly surpassed by gravitational forces (Niemann and Hasbargen, 2005). According to these criteria, the model is not perfectly dynamically scaled compared to natural systems. Nevertheless, the balance among the different forces in nature appears to be preserved in the model: gravitational forces dominate, while inertial forces typically exceed viscous forces. Moreover, the morphometric characterization of the channels in our experiments (Fig. 16d) closely resembles that of natural rivers in comparable tectonic and climatic settings (e.g., Guerit et al., 2018).

4.2 Strengths and limitations of the experimental approach

Analog modeling cannot fully replicate the complexity of all natural processes and associated complex interactions that govern relief dynamics. That said, meaningful and relevant results, validated by morphometric comparisons between the model and natural topographies, can be obtained using this experimental approach. Despite the semi-empirical basis and uncertainties of constitutive parameters (discussed in section 2.4), geomorphic model scaling yields consistent results. The concept of auto-similarity is often evoked to explain the striking analogy between experimental morphologies and their natural counterparts (e.g., Paola et al., 2009; Reber et al., 2020). However, as with any modeling approach, limitations exist and must be carefully considered when extrapolating model results to natural systems.

4.2.1 Simulate long-term evolution

Natural landscapes result from morpho-tectonic evolution spanning several million years, during which slow and fast morphogenetic processes interact and shape the landscapes. Based on the previously evaluated time scaling, simulating such long-term evolution would require experiment duration of a week or more, which is technically feasible, but logistically challenging. Setting up an initial topography based on a natural DEM reference only partially compensates for this issue. First, it is technically challenging to reproduce natural morphologies with a high level of detail manually. Second, it is unlikely that the model would maintain the same state of dynamic equilibrium that has shaped the initial topography over the past million years.

4.2.2 Diffusion/incision competition

Despite significant improvements in erodibility and morphological fineness, the geomorphic properties of MAT-V still show some areas for improvement. One commonly observed issue is that hillslopes deliver a large amount of non-channelized sediments to the drainage network, saturating the river's transport capacity and, consequently, promoting lateral erosion over river incision. The competition between slope diffusion and river incision appears to be a key parameter controlling the morphological evolution of both natural and experimental landscapes. Several strategies can be used to adjust this balance:

- Increasing the cohesion of MAT-V by raising the proportion of silica powder relative to microbeads (EXP 8, where Psi/Mb = 1.5 ; see Fig. 3) increases the critical slope, thereby reducing the effectiveness of slope diffusion processes and enhancing river incision. Because a stronger material is harder to erode by non-channelized water flows, this typically results in the formation of dissected plateau evolving into badlands-like morphologies (preserved surfaces dissected by deep incised channels). However, increasing material cohesion also alters the tectonic style, making the material excessively brittle.

- Using rainfall cycles rather than continuous rainfall is an efficient way to enhance river incision. During the wet period, water runoffs spreads across the whole model surface, triggering both slope diffusion and river transport, incision, or aggradation. At the onset of the dry period, slope diffusion processes ceases almost instantaneously while water continues to flow in the drainage network for several seconds (up to 10 s for large models). With less sediment coming from the slopes, the transport and incision capacity of the rivers increases, leading to more entrenched channels. Notably, in the model presented, water flows in the drainage network don't stop totally, even when rainfall cycles include a dry period of 20 s.

4.2.3 Transport distance

Despite the presence of low-density (<1.5) grains, such as PVC powder, pumice powder, and anthracite, the MAT-V composition is dominated by high intrinsic density (~2.5) silica particles (silica powder and microbeads). These denser particles tend to reduce the transport distance of eroded material by a factor of

about 2, as inferred from the length/thickness ratio of natural alluvial fans. This discrepancy is difficult to compensate for, except maybe by using saline water in the rainfall system to increase the buoyancy of MAT-V particles.

4.2.4 Time of response

All these limitations can impact the dynamic equilibrium of the model's topography by disrupting the response times of some surface processes to autogenic or allogenic forcing. For example, while knickpoints formation is well-simulated, knickpoints migrate upstream rather slowly considering the model's time scaling.

4.2.5 Material stratification

To date, most geomorphic experiments performed with the MAT-IV and MAT-V analog materials have been done without reproducing the layering characterizing natural sedimentary formations. This certainly has an impact on the morphology of the model's surface, but more importantly on its mechanical behavior. In Graveleau (2008, Figure III.40), Graveleau et al. (2011, reproduced here in Fig. 17), we demonstrated that alternating centimetric layers of MAT-IV with millimetric layers of low internal friction microbeads reduces bulk material strength, enhances plastic strain (folding), while promoting the propagation of the brittle deformation (faulting).

All these observations are helpful not only for adapting the tectonic style but also for refining the morphology. As previously mentioned, the MAT-V standard composition (37.5% PSi, 37.5% Mb, 15% PVC, 10% Pp, and 1% A) may have a diffusion coefficient that is too high, which limits river incision capacitiy. Using a more cohesive formulation (40% PSi, 35% Mb, 15% PVC, 10% Pp, and 1% A) improved this issue but made the analog material too brittle, degrading the overall tectonic deformation style. One solution would be to interstratify layers of this more cohesive MAT-V formulation with a weaker material such as silica microbeads or even PVC powder (as previously tested with MAT-IV, Fig. 17) to improve the interplay between slope diffusion and river incision and decrease the bulk material resistance.

4.3 Strengths and limitations of the numerical modeling approach

The numerical approach developed using the Landlab Python library successfully replicated the slope distribution, drainage density, and erosion rate observed in the experimental models (Figs. 11 and 12) and offers a powerful tool for advancing our understanding of erosive processes, in particular for assessing parameters such as the substrate erodibility, the discharge exponent, the hillslope erodibility or the critical slope. However, computation time remains the main technical limitation. The numerical models are discretized into 101x101 grid (10,201 nodes) and launched with 2,000–12,000 time steps, resulting in computation times of 5–30 minutes per simulation. Running tens or hundreds of thousands of models takes several weeks or months and requires substantial computing resources, even using Python multiprocessing modules.

Landlab's open-source nature provides considerable flexibility. Users can combine pre-existing process components or implement custom formulations to develop specific geomorphic laws. Numerical model we employed uses existing laws for fluvial incision (Davy and Lague, 2009) and hillslope processes (Carretier et al., 2016). To reduce model complexity and associated computing time, we made two main simplifications. First, we considered end-member models assuming no critical stream power threshold to erode substrate. While Ferguson (2005, 2012) proposed a method to estimate this threshold based on grain size and hydraulic roughness, its value varies widely across natural environments. Second, we decided not to integrate a law for lateral erosion. This law is available in Landlab via the "LateralEroder" function (Langston and Tucker, 2018) but requires setting additional parameters describing the potential for deposition and the lateral-to-vertical bedrock erodibility ratio that are, to date, difficult to assess. As a result, our models cannot simulate channel widening beyond the mesh resolution; valley widening occurs only indirectly through the convergence of nearby drainages. The numerical approach described in section 3.3 focused on modeling an erosion box without tectonic forcing. However, to make the approach more widely applicable, numerical models should be capable of simulating surface processes and tectonic deformation. The current version of Landlab only allows for vertical and normal faulting and associated block uplift or subsidence. It does not yet include tectonically-induced surface deformation resulting from folding or reverse faulting. Future numerical developments are needed to reproduce the complexity of tectonic forcing and integrate natural morphogenetic processes and couplings.

4.4 Joint analog/numerical modeling approach

Analog and numerical approaches are highly complementary, each offering unique advantages and limitations. Analog models take a long time to set up and require robust scaling to relate experimental outcomes to real-world observations. Thanks to the use of granular materials with very fine particle sizes, analog models allow for highly detailed morphometric analyses over large spatial scales, often at meter resolution. Conversely, numerical models can be conducted directly at natural scale and permit rapid testing of variations in boundary conditions. Yet, they are constrained by computational limits on mesh resolution, which restrict the modeling of morphological structures smaller than several tens of meters. The joint analog–numerical approach developed in this study is innovative and highly promising. On the one hand, numerical modeling enables us to characterize parameters associated with MAT-V that are difficult to assess in the lab, such as the settling velocity, the discharge exponent, the hill-

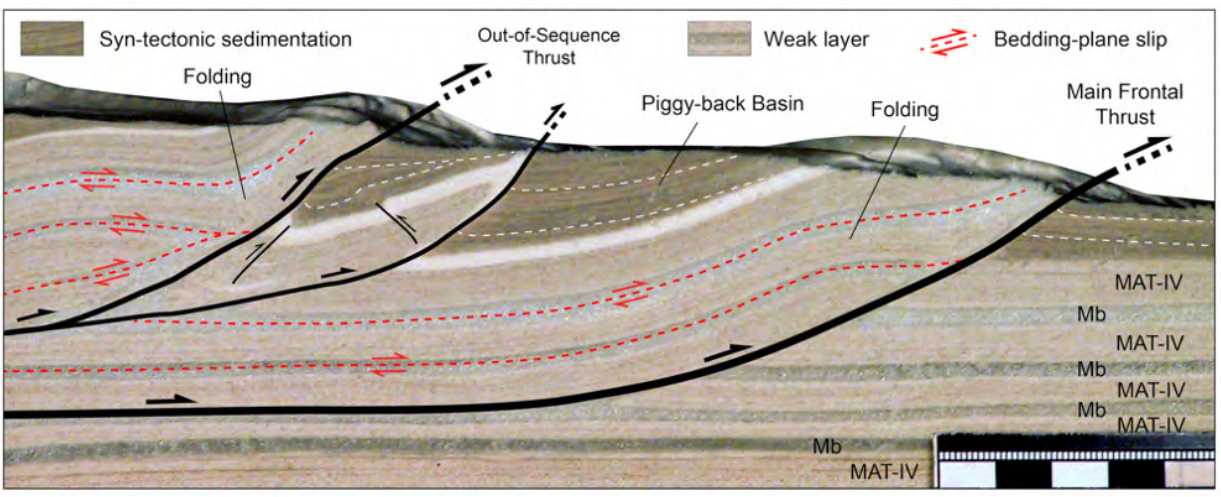

Figure 17 Example of tectonic style obtained using stratified MAT-IV material (cross-section). The model deforms through faulting, folding, bedding-plane slip, underthrusting, and the activation of out-of-sequence thrusts. Modified from Graveleau (2008).

slope erodibility, and the critical slope. On the other hand, analog modeling enables us to test the relevance of the erosion laws used in numerical models by providing a framework with known initial geometry, boundary conditions, and climatic and tectonic forcings. This integrated strategy offers a powerful tool for improving our understanding of tectonic–erosion couplings and enhances the interpretation of natural landform evolution by bridging the gap between detailed physical processes and large-scale landscape dynamics.

5 Conclusions

MAT-V is a promising analog material that could advantageously replace MAT-IV, developed over a decade ago, to perform geomorphic experiments investigating relief dynamics in a wide range of tectonic contexts. Modifications made to its composition resulted in physical and mechanical properties that have improved the morphological rendering and extended its field of applications, notably to the short time scale of the seismic cycle.

Reducing the grain size of MAT-V components led to a significant shift in bulk granulometry compared with MAT-IV (D_{50} reduced from 105 µm to 50 µm). This change enhanced slope diffusion, channel incision, and material transport. It has also improved the fineness of the modeled morphologies (drainage network, crest lines, alluvial deposits, and tectonic structures). The addition of pumice powder (Pp) also contributed to increasing MAT-V erodibility. The microporosity of the Pp grains promotes water retention within the material, enhancing the loss of material cohesion induced by water runoff.

By generating rainfall cycles, it becomes possible to simulate specific climatic boundary conditions and adjust erosion rates. Alternating wet and dry periods influence the competition between slope diffusion and fluvial incision processes, promoting deeper stream entrenchment compared to continuous rainfall conditions. Notably, MAT-V erodes 3 to 4 times faster than MAT-IV, under rainfall rates that are 3 to 4 times lower. This allows for daily experiments representing longer geological spans than MAT-IV, while using smaller and better-scaled water flows.

Qualitative and quantitative comparisons between model and natural morphologies, based on morphometric criteria, led to the following recommended standard MAT-V composition: Mb: 37.5%, Si: 37.5%, PVC: 15%, Pp: 10%, Anthracite: $\leq$1%. Using this recipe and an average cyclic rainfall rate of about 5–10 mm/h, a spatial scaling of 1 cm = 100 m and 1 s = 3–5 years can be considered relevant to model relief dynamics in temperate to sub-tropical climatic conditions. Spatial and temporal scaling are strongly influenced by the physical and mechanical properties of the analog material, as well as by the applied boundary conditions, such as imposed deformation kinematics and rainfall rate. Due to the variable particle densities and cohesion values of wet granular mixtures, typically ranging from 1.2 to 2.7 g/cm^3 and 500 to 5000 Pa, respectively, such analog materials are best suited for simulating natural systems at kilometric scales over timescales of a few million years. Taking this information into account, model scaling could easily be adapted to specific morpho-tectonic settings by 1) changing the relative proportions of the MAT-V components to modify its mechanical and geomorphic properties and/or 2) adjusting the rainfall rate and cycle parameters.

Finally, the methodological approach of combining experimental and numerical modeling has proven highly effective for constraining parameters that are difficult to assess experimentally. Using this approach, the MAT-V geomorphic parameters related to river incision and hillslope processes were well constrained, thereby providing key parameters for further adaptation of the MAT-V scaling to specific tectono-climatic settings. Concurrently, some issues related to the numerical simulation of morphotectonic processes, such as lateral river erosion and the surface expression of faulting, have been identified and are currently being addressed. This mutually beneficial approach is certainly expected to develop further in the coming years, supported by continuous improvements in computational performance and advances in our understanding

of geomorphic process dynamics.

Acknowledgements

We thank the anonymous reviewers for their constructive comments and suggestions that improved the manuscript. Thanks to Christian Romano and Stéphane Arnal (GM-UM) for providing expert technical support. Thanks to Martine Trautmann (LAS-UNISTRA-EOS) for the granulometric measurements and Frédéric Fernandez (MEA-University of Montpellier) for the Scanning Electron Microscopy photographs and Energy Dispersive X-ray micro-analysis. The Landlab software (Barnhart et al., 2020) was used to model the analog erosion box experiments numerically. The maps and graphics presented in this study were generated using the Generic Mapping Tools (GMT) software (Wessel and Smith, 1998; Wessel et al., 2013).

Land Recognition

After consulting relevant resources and checking with the relevant local communities, the authors have confirmed that the lands containing their institutions and all work sites associated with this study do not have cultural or historical significance to a particular indigenous group.

Data and Codes Availability

Code and data are available on a Zenodo repository under Creative Commons Attribution 4.0 International: Dominguez (2025) https://doi.org/10.5281/zenodo.17692013

Funding Statement

This study was funded by the CNRS-INSU-Tellus programs, the University of Montpellier (UM), and the ANR TopoExtreme project (ANR-18-CE01-0017).

Conflict of Interest Disclosure

The authors have no competing interests.

Permission to Reproduce Material from Copyrighted Sources

The authors declare that no material from copyrighted sources was reproduced in this manuscript.

Declaration on Artificial Intelligence Use

The authors declare that no artificial intelligence tool was used to assist in or generate any part of the contents in this manuscript. Authors used large language models (LLM), such as DeepL and Grammarly, to assist with English grammar and language.

References

Al-Hashemi, H. and Al-Amoudi, O. A. A review on the angle of repose of granular materials. *Powder Technology*, 330:397–417, 2018. doi: 10.1016/j.powtec.2018.02.003.

Babault, J., Bonnet, S., Crave, A., and van den Driessche, J. Influence of piedmont sedimentation on erosion dynamics of an uplifting landscape: An experimental approach. *Geology*, 33(4): 301–304, 2005a. doi: 10.1130/G21095.1.

Babault, J., Van Den Driessche, J., Bonnet, S., Castelltort, S., and Crave, A. Origin of the highly elevated Pyrenean peneplain. *Tectonics*, 24:TC2010, 2005b. doi: 10.1029/2004TC001697.

Barnhart, K., Glade, R., Shobe, C., and Tucker, G. Terrainbento 1.0: A Python package for multi-model analysis in long-term drainage basin evolution. *Geoscientific Model Development*, 12 (4):1267–1297, 2019. doi: 10.5194/gmd-12-1267-2019.

Barnhart, K. R., Hutton, E. W. H., Tucker, G. E., Gasparini, N. M., Istanbulluoglu, E., Hobley, D. E. J., Lyons, N. J., Mouchene, M., Nudurupati, S. S., Adams, J. M., and Bandaragoda, C. Short communication: Landlab v2.0: A software package for Earth surface dynamics. *Earth Surface Dynamics*, 8(2):379–397, 2020. doi: 10.5194/esurf-8-379-2020.

Beaumont, C. The evolution of sedimentary basins on a viscoelastic lithosphere: Theory and examples. *Geophysical Journal International*, 55(2):471–497, 1978. doi: 10.1111/j.1365-246X.1978.tb04283.x.

Beaumont, C., Fullsack, P., and Hamilton, J. Erosional control of active compressional orogens. In *Thrust Tectonics*, edited by McClay, K. R. Springer, Dordrecht, 1992. doi: 10.1007/978-94-011-3066-0_1.

Bishop, P. Long-term landscape evolution: Linking tectonics and surface processes. *Earth Surface Processes and Landforms*, 32: 329–365, 2007. doi: 10.1002/esp.1493.

Blair, T. C. and McPherson, J. G. Processes and forms of alluvial fans. In *Geomorphology of Desert Environments*, edited by Parsons, A. J. and Abrahams, A. D. Springer, Dordrecht, 2009. doi: 10.1007/978-1-4020-5719-9_14.

Bonnet, C., Malavieille, J., and Mosar, J. Interactions between tectonics, erosion, and sedimentation during the recent evolution of the Alpine orogen: Analogue modeling insights. *Tectonics*, 26: TC6016, 2007. doi: 10.1029/2006TC002048.

Bonnet, S. and Crave, A. Landscape response to climate change: Insights from experimental modeling and implications for tectonic versus climatic uplift of topography. *Geology*, 31:123–136, 2003. doi: 10.1130/0091-7613(2003)031<0123:LRTCCI>2.0.CO;2.

Burbank, D. and Pinter, N. Landscape evolution: The interactions of tectonics and surface processes. *Basin Research*, 11: 1–6, 1999. doi: 10.1046/j.1365-2117.1999.00089.x.

Byerlee, J. Friction of rock. *Pure and Applied Geophysics*, 116: 615–626, 1978. doi: 10.1007/BF00876528.

Caniven, Y., Dominguez, S., Soliva, R., Cattin, R., Peyret, M., Marchandon, M., Romano, C., and Strak, V. A new multilayered visco-elasto-plastic experimental model to study strike-slip fault seismic cycle. *Tectonics*, 34:232–264, 2015. doi: 10.1002/2014TC003701.

Carretier, S., Martinod, P., Reich, M., and Godderis, Y. Modelling sediment clasts transport during landscape evolution. *Earth Surface Dynamics*, 4(1):237–251, 2016. doi: 10.5194/esurf-4-237-2016.

Charreau, J., Saint-Carlier, D., Lavé, J., Dominguez, S., Blard, P.-H., Avouac, J.-P., Brown, N. D., Malatesta, L. C., Wang, S., and Rhodes, E. J. Late Pleistocene acceleration of deformation across the northern Tianshan piedmont (China)

evidenced from the morpho-tectonic evolution of the Dushanzi anticline. *Tectonophysics*, 730:132–140, 2018. doi: 10.1016/j.tecto.2018.02.016.

Chaudhry, M. H. *Open-Channel Flow*. Springer, New York, 2 edition, 2008. doi: 10.1007/978-3-030-96447-4.

Conrad, E. M., Reitano, R., Faccenna, C., and Becker, T. W. Morpho-tectonics of transpressional systems: Insights from analog modeling. *Tectonics*, 42(10), 2023. doi: 10.1029/2023TC007865.

Crosby, B. T. and Whipple, K. X. Knickpoint initiation and distribution within fluvial networks: 236 waterfalls in the Waipaoa River, North Island, New Zealand. *Geomorphology*, 82(1-2), 2006. doi: 10.1016/j.geomorph.2005.08.023.

Davy, P. and Cobbold, P. R. Experiments on shortening of a 4-layer model of the continental lithosphere. *Tectonophysics*, 188:1–25, 1991. doi: 10.1016/0040-1951(91)90311-F.

Davy, P. and Lague, D. Fluvial erosion/transport equation of landscape evolution models revisited. *Journal of Geophysical Research: Earth Surface*, 114:F03007, 2009. doi: 10.1029/2008JF001146.

Dominguez, S. DATASETS associated to the manuscript published in GEOMORPHICA: Physical and Mechanical Properties of a New Analog Material (MAT-V) for Geomorphic Experiments, 2025, Data set. doi:10.5281/zenodo.17692013.

East, A. E. and Sankey, J. B. Geomorphic and sedimentary effects of modern climate change: Current and anticipated future conditions in the western United States. *Reviews of Geophysics*, 58: e2019RG000692, 2020. doi: 10.1029/2019RG000692.

Ferguson, R. I. Estimating critical stream power for bedload transport calculations in gravel-bed rivers. *Geomorphology*, 70(1-2): 33–41, 2005. doi: 10.1016/j.geomorph.2005.03.009.

Ferguson, R. I. River channel slope, flow resistance, and gravel entrainment thresholds. *Water Resources Research*, 48:W05517, 2012. doi: 10.1029/2011WR010850.

Garcia-Castellanos, D. and Cloetingh, S. Modeling the interaction between lithospheric and surface processes in foreland basins. In *Tectonics of Sedimentary Basins: Recent Advances*, edited by Busby, C. and Azor, A., pages 152–181. Blackwell Publishing Ltd., 2012. doi: 10.1002/9781444347166.ch8.

Grant, F. S. and West, G. F. *Interpretation Theory in Applied Geophysics*. McGraw-Hill, New York, 1965.

Graveleau, F. *Interactions Tectonique, Erosion, Sédimentation dans les avant-pays de chaînes : Modélisation analogique et étude des piémonts de l'est du Tian Shan (Asie centrale)*. PhD thesis, Université Montpellier II - Sciences et Techniques du Languedoc, 2008. In French. tel-00339145v2.

Graveleau, F. and Dominguez, S. Analogue modelling of the interaction between tectonics, erosion and sedimentation in foreland thrust belts. *Comptes Rendus Geoscience*, 340:324–333, 2008. doi: 10.1016/j.crte.2008.01.005.

Graveleau, F., Hurtrez, J.-E., Dominguez, S., and Malavieille, J. A new experimental material for modelling relief dynamics and interactions between tectonics and surface processes. *Tectonophysics*, 513(1-4):68–87, 2011. doi: 10.1016/j.tecto.2011.09.029.

Graveleau, F., Malavieille, J., and Dominguez, S. Experimental modelling of orogenic wedges: A review. *Tectonophysics*, 538-540:1–66, 2012. doi: 10.1016/j.tecto.2012.01.027.

Graveleau, F., Strak, V., Dominguez, S., Malavieille, J., Chatton, M., Manighetti, I., and Petit, C. Experimental modelling of tectonics–erosion–sedimentation interactions in compressional, extensional, and strike-slip settings. *Geomorphology*, 244:146–168, 2015. doi: 10.1016/j.geomorph.2015.02.011.

Guerit, L., Dominguez, S., Malavieille, J., and Castelltort, S. Deformation of an experimental drainage network in oblique collision. *Tectonophysics*, 693:210–222, 2016. doi: 10.1016/j.tecto.2016.04.016.

Guerit, L., Goren, L., Dominguez, S., Malavieille, J., and Castelltort, S. Landscape stress and reorganization from chi-maps: Insights from experimental drainage networks in oblique collision setting. *Earth Surface Processes and Landforms*, 43:3152–3163, 2018. doi: 10.1002/esp.4477.

Harel, M.-A., Mudd, S. M., and Attal, M. Global analysis of the stream power law parameters based on worldwide 10Be denudation rates. *Geomorphology*, 268:184–196, 2016. doi: 10.1016/j.geomorph.2016.05.035.

Henriquet, M., Dominguez, S., Barreca, G., Malavieille, J., Cadio, C., and Monaco, C. Deep origin of the dome-shaped Hyblean Plateau, southeastern Sicily: A new tectono-magmatic model. *Tectonics*, 38:184–196, 2019. doi: 10.1029/2019TC005548.

Hobley, D. E. J., Adams, J. M., Nudurupati, S. S., Hutton, E. W. H., Gasparini, N. M., Istanbulluoglu, E., and Tucker, G. E. Creative computing with Landlab: An open-source toolkit for building, coupling, and exploring two-dimensional numerical models of Earth-surface dynamics. *Earth Surface Dynamics*, 5(1):21–46, 2017. doi: 10.5194/esurf-5-21-2017.

Hoek, E. and Brown, E. T. The Hoek-Brown failure criterion – a 1988 update. In *Proceedings of the 15th Canadian Rock Mechanics Symposium*, pages 31–38, 1988.

Hoek, E. and Brown, E. T. Practical estimates of rock mass strength. *International Journal of Rock Mechanics and Mining Sciences*, 34 (8):1165–1186, 1997. doi: 10.1016/S1365-1609(97)80069-X.

Hovius, N. Regular spacing of drainage outlets from linear mountain belts. *Basin Research*, 8(1):29–44, 1996. doi: 10.1046/j.1365-2117.1996.01491.x.

Hubbert, M. K. Theory of scale models as applied to the study of geologic structures. *Geological Society of America Bulletin*, 48: 1459–1520, 1937. doi: 10.1130/GSAB-48-1459.

Huggett, R. *Fundamentals of Geomorphology*. Routledge, 4 edition, 2016. doi: 10.4324/9781315674179.

Jolivet, J., Barrier, L., Dominguez, S., Guerit, L., Heilbronn, G., et al. Unbalanced sediment budgets in the catchment-alluvial fan system of the Kuitun River (northern Tian Shan, China): Implications for mass-balance estimates, denudation and sedimentation rates in orogenic systems. *Geomorphology*, 214: 168–182, 2014. doi: 10.1016/j.geomorph.2014.01.024.

Konstantinovskaia, E. and Malavieille, J. Erosion and exhumation in accretionary orogens: Experimental and geological approaches. *Geochemistry, Geophysics, Geosystems*, 6:Q02006, 2005. doi: 10.1029/2004GC000794.

Krantz, R. W. Measurements of friction coefficients and cohesion for faulting and fault reactivation in laboratory models using sand and sand mixtures. *Tectonophysics*, 188:203–207, 1991. doi: 10.1016/0040-1951(91)90323-K.

Lague, D., Crave, A., and Davy, P. Laboratory experiments simulating the geomorphic response to tectonic uplift. *Journal of Geophysical Research*, 108(B1):1–20, 2003. doi: 10.1029/2002JB001785.

Langston, A. L. and Tucker, G. E. Developing and exploring a theory for the lateral erosion of bedrock channels for use in landscape evolution models. *Earth Surface Dynamics*, 6(1):1–27, 2018. doi: 10.5194/esurf-6-1-2018.

Malavieille, J. Impact of erosion, sedimentation, and structural heritage on the structure and kinematics of orogenic wedges: Analog models and case studies. *GSA Today*, 20:4–10, 2010. doi: 10.1130/GSATG48A.1.

Mao, Y., Li, Y., Yan, B., Wang, X., Jia, D., and Chen, Y. Response of surface erosion to crustal shortening and its influ-

ence on tectonic evolution in fold-and-thrust belts: Implications from sandbox modeling. *Tectonics*, 40:1–26, 2021. doi: 10.1029/2020TC006515.

Montgomery, D. R. and Brandon, M. T. Topographic controls on erosion rates in tectonically active mountain ranges. *Earth and Planetary Science Letters*, 201(3–4):481–489, 2002. doi: 10.1016/S0012-821X(02)00725-2.

Mugnier, J.-L., Baby, P., Colletta, B., Vinour, P., Bale, P., and Leturmy, P. Thrust geometry controlled by erosion and sedimentation: A view from analogue models. *Geology*, 25:427–430, 1997. doi: 10.1130/0091-7613(1997)025<0427:TGCBEA>2.3.CO;2.

Niemann, J. D. and Hasbargen, L. E. A comparison of experimental and natural drainage basin morphology across a range of scales. *Journal of Geophysical Research: Earth Surface*, 110: F04017, 2005. doi: 10.1029/2004JF000204.

Paola, C., Straub, K., Mohrig, D., and Reinhardt, L. The "unreasonable effectiveness" of stratigraphic and geomorphic experiments. *Earth-Science Reviews*, 97:1–4, 2009. doi: 10.1016/j.earscirev.2009.05.003.

Philip, H. and Meghraoui, M. Structural analysis and interpretation of the surface deformations of the El Asnam earthquake of October 10, 1980. *Tectonics*, 2(1):17–49, 1983. doi: 10.1029/TC002i001p00017.

Ramberg, H. *Gravity, Deformation and the Earth's Crust: In Theory, Experiments and Geological Application*. Academic Press, 1981.

Reber, J. E., Cooke, M. L., and Dooley, T. P. What model material to use? A review on rock analogs for structural geology and tectonics. *Earth-Science Reviews*, 202:103107, 2020. doi: 10.1016/j.earscirev.2020.103107.

Reitano, R., Faccenna, C., Funiciello, F., Corbi, F., and Willett, S. D. Erosional response of granular material in landscape models. *Earth Surface Dynamics*, 8(4):973–993, 2020. doi: 10.5194/esurf-8-973-2020.

Reitano, R., Faccenna, C., Funiciello, F., Corbi, F., Sternai, P., Willett, S. D., et al. Sediment recycling and the evolution of analog orogenic wedges. *Tectonics*, 41:1–17, 2022. doi: 10.1029/2021TC006951.

Reitano, R., Clementucci, R., Conrad, E. M., Corbi, F., Lanari, R., Faccenna, C., and Bazzucchi, C. Stream laws in analog tectonic-landscape models. *Earth Surface Dynamics*, 11:731–740, 2023. doi: 10.5194/esurf-11-731-2023.

Roering, J. J., Kirchner, J. W., and Dietrich, W. E. Evidence for nonlinear, diffusive sediment transport on hillslopes and implications for landscape morphology. *Water Resources Research*, 35 (3):853–870, 1999. doi: 10.1029/1998WR900090.

Rohais, S., Bonnet, S., and Eschard, R. Sedimentary record of tectonic and climatic erosional perturbations in an experimental coupled catchment-fan system. *Basin Research*, 24:198–212, 2012. doi: 10.1111/j.1365-2117.2011.00520.x.

Rosenau, M., Corbi, F., and Dominguez, S. Analogue earthquakes and seismic cycles: Experimental modelling across timescales. *Solid Earth*, 8:597–635, 2017. doi: 10.5194/se-8-597-2017.

Rupnik, E., Daakir, M., and Pierrot-Deseilligny, M. MicMac – a free, open-source solution for photogrammetry. *Open Geospatial Data, Software and Standards*, 2:14, 2017. doi: 10.1186/s40965-017-0027-2.

Scheingross, J. S., Limaye, A. B., McCoy, S. W., et al. The shaping of erosional landscapes by internal dynamics. *Nature Reviews Earth & Environment*, 1:661–676, 2020. doi: 10.1038/s43017-020-0096-0.

Schellart, W. P. and Strak, V. A review of analogue modelling of geodynamic processes: Approaches, scaling, materials and quantification, with an application to subduction experiments. *Journal of Geodynamics*, 100:7–32, 2016. doi: 10.1016/j.jog.2016.03.009.

Steer, P., Simoes, M., Cattin, R., et al. Erosion influences the seismicity of active thrust faults. *Nature Communications*, 5:5564, 2014. doi: 10.1038/ncomms6564.

Strak, V. *L'évolution du relief le long des escarpements de faille normale active : observations, modélisations expérimentales et numériques*. PhD thesis, Université Pierre et Marie Curie - Paris VI, 2012. In French. NNT: 2012PA066289. tel-00750065.

Strak, V., Dominguez, S., Petit, C., Meyer, B., and Loget, N. Interaction between normal fault slip and erosion on relief evolution: Insights from experimental modelling. *Tectonophysics*, 513:1–19, 2011. doi: 10.1016/j.tecto.2011.10.005.

Strzerzynski, P., Dominguez, S., Boudiaf, A., and Déverchère, J. Tectonic inversion and geomorphic evolution of the Algerian margin since Messinian times: Insights from new onshore/offshore analog modeling experiments. *Tectonics*, 40:1–26, 2021. doi: 10.1029/2020TC006369.

Tucker, G., Catani, F., Rinaldo, A., and Bras, R. Statistical analysis of drainage density from digital terrain data. *Geomorphology*, 36 (3–4):187–202, 2001. doi: 10.1016/S0169-555X(00)00056-8.

Tucker, G. E. and Hancock, G. R. Modelling landscape evolution. *Earth Surface Processes and Landforms*, 35:28–50, 2010. doi: 10.1002/esp.1952.

Van Puymbroeck, N., Rémi, M., Binet, R., Avouac, J.-P., and Taboury, J. Measuring earthquakes from optical satellite images. *Applied Optics*, 39:3486–3494, 2000. doi: 10.1364/AO.39.003486.

Viaplana-Muzas, M., Babault, J., Dominguez, S., Van Den Driessche, J., and Legrand, X. Drainage network evolution and patterns of sedimentation in an experimental wedge. *Tectonophysics*, 664: 109–124, 2015. doi: 10.1016/j.tecto.2015.09.007.

Viaplana-Muzas, M., Babault, J., Dominguez, S., Van Den Driessche, J., and Legrand, X. Modelling of drainage dynamics influence on sediment routing system in a fold-and-thrust belt. *Basin Research*, 31:290–310, 2018. doi: 10.1111/bre.12321.

Watts, A. B., Karner, G. D., and Steckler, M. S. Lithospheric flexure and the evolution of sedimentary basins. *Philosophical Transactions of the Royal Society of London A*, 305(1489):249–281, 1982.

Weijermars, R. and Schmeling, H. Scaling of Newtonian and non-Newtonian fluid dynamics without inertia for quantitative modelling of rock flow due to gravity. *Physics of the Earth and Planetary Interiors*, 43(4):316–330, 1986. doi: 10.1016/0031-9201(86)90021-X.

Wessel, P. and Smith, W. H. F. New, improved version of generic mapping tools released. *Eos, Transactions American Geophysical Union*, 79(47):579–579, 1998. doi: 10.1029/98EO00426.

Wessel, P., Smith, W. H. F., Scharroo, R., Luis, J., and Wobbe, F. Generic Mapping Tools: Improved Version Released. *Eos Trans*, 94(45):409, 2013. doi: 10.1002/2013EO450001.

Whipple, K. The influence of climate on the tectonic evolution of mountain belts. *Nature Geoscience*, 2(2):97–104, 2009. doi: 10.1038/ngeo413.

Whipple, K., Kirby, E., and Brocklehurst, S. Geomorphic limits to climate-induced increases in topographic relief. *Nature*, 401: 39–43, 1999. doi: 10.1038/43375.

Whipple, K. X. and Tucker, G. E. Dynamics of the stream power river incision model: Implications for height limits of mountain ranges, landscape response timescales and research needs. *Journal of Geophysical Research*, 104(B8):17661–17674, 1999. doi: 10.1029/1999JB900120.

Whittaker, A. and Boulton, S. Tectonic and climatic controls on

knickpoint retreat rates and landscape response times. *Journal of Geophysical Research: Earth Surface*, 117:F02024, 2012. doi: 10.1029/2011JF002157.

Willett, S. D. Orogeny and orography: The effects of erosion on the structure of mountain belts. *Journal of Geophysical Research*, 104(B2):28957–28981, 1999. doi: 10.1029/1999JB900248.

Willett, S. D., Beaumont, C., and Fullsack, P. Mechanical model for the tectonics of doubly vergent compressional orogens. *Geology*, 21(4):371–374, 1993. doi: 10.1130/0091-7613(1993)021<0371:MMFTTO>2.3.CO;2.

edited by Willett, S. D., Hovius, N., Brandon, M. T., and Fisher, D. *Tectonics, Climate and Landscape Evolution*, volume 398 of *Special Paper*. Geological Society of America, 2006. doi: 10.1130/SPE398.

Yan, B., Jia, D., and Wang, M. Drainage development on the northern Tibetan Plateau controlled by the Altyn Tagh Fault: Insights from analogue modelling. *Earth Surface Processes and Landforms*, 48, 2023. doi: 10.1002/esp.5600.